Master of Science Thesis

STEREOID Data Processor: Design and Performance Analysis

Prithvi Laguduvan Thyagarajan

TUDelft
Delft
University of
Technology

STEREOID DATA PROCESSOR : DESIGN AND PERFORMANCE ANALYSIS

A thesis submitted to the Delft University of Technology in partial fulfillment
of the requirements for the degree of

Master of Science in Electrical Engineering

by

Prithvi Laguduvan Thyagarajan

October 2019
This thesis can be found in the TU Delft repository: https://repository.tudelft.nl

The work in this thesis was made in collaboration with:

Microwave, Sensing, Signals and Systems
Faculty of Electrical Engineering, Mathematics and Computer Science
Civil Engineering, Geosciences and Remote Sensing
Delft University of Technology

Supervisors: Prof.dr. Alexander Yarovoy
Dr. Paco Lopez Dekker
Dr. Yuanhao Li and Dr. Lorenzo Iannini

ACKNOWLEDGEMENTS

ABSTRACT

Stereo Thermo-Optically Enhanced Radar for Earth, Ocean, Ice, and land Dynamics (STEREOID) is one of the candidates of the ESA (European Space Agency) , Earth Explorer 10 missions. The novel constellation system will consist of the active Sentinel-1 satellites and two passive spacecrafts , which can provide flexible baseline configurations. The main objective of the mission lies in monitoring the variation of spatially diverse ice sheets, the eruptions of earthquakes, the volcano activities, and the landslides, playing therefore an extremely important role in understanding the global climate dynamics and the geophysical processes involved.

The purpose of the thesis is to develop an end-to-end simulator incorporating the STEREOID bistatic configuration operating in TOPS (Terrain Observation by Progressive Scans) mode and evaluate its performance. To achieve this goal, the key component of the simulator, the SAR (Synthetic Aperture Radar) processing kernel was first implemented. The kernel employs an imaging algorithm which assists in image formation and focusing for different bistatic geometries generated by relevant working modes of the STEREOID mission. This is further extended to bistatic TOPS acquisition mode with azimuth beamforming under dual antenna receiver configuration of STEREOID. The performance of STEREOID mission is evaluated under different bistatic geometries and the dual beamforming stratergy is evaluated for parameters such as resolution, pointing errors and gain imbalances. This is evaluated to analyse and understand the importance of calibration errors introduced into the system.

CONTENTS

1 | INTRODUCTION

1.1 INTRODUCTION TO SYNTHETIC APERTURE RADAR

Synthetic Aperture Radar (SAR) is a class of radar which can produce high resolution, 2 or 3 dimensional images of an area of interest. SAR is generally mounted on an aircraft for satellite of constant velocity. It is found in various applications but the main application concentrated in this thesis is remote sensing. A few reasons for SAR to be used in remote sensing is mainly due to the nature of the sensor. Firstly, SAR operates in its own illumination and thus can also operate in the darkness. Secondly, the radar waves scatter off objects more differently than a conventional optical sensor. Hence, SAR provides more information about the characteristics of a target of interest. Lastly, the electromagnetic waves in the radio frequency range can penetrate through clouds, fog, mist and precipitation.

SAR images the earth surface from a satellite by transmitting phase encoded pulses perpendicular to the sensor and receiving the reflection of the signal from the target of interest. When a two dimensional image is formed, one dimension, the x axis, is parallel to the radar beam and the next dimension, the y axis, is parallel to the motion of the sensor. The Fig. 1.1 depicts a simple SAR system geometry explaining the range and azimuth directions of a SAR system. The x axis consists of the radar echo placed at the right distance from the sensor. Since the beam is not parallel to the ground, converting a 3D image to 2D results in a geometric distortion which is eventually corrected during processing. The received echo signals are processed along the azimuth time. This stage occurs when the sensor points in a straight line to the earth and the radar scans the earth at approximately the same speed.
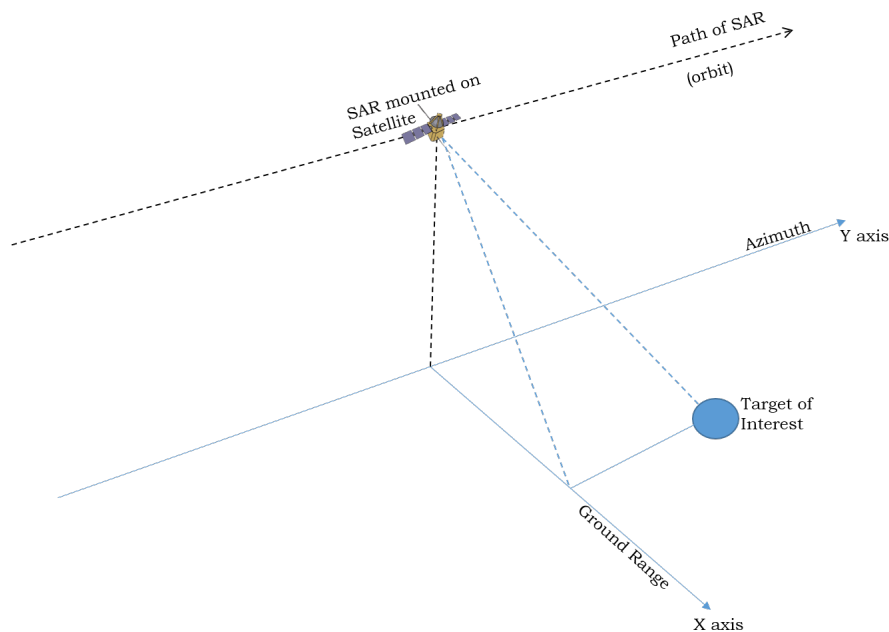
Figure 1.1: A simple geometry of SAR System

1.1.1 Modes of operation in SAR

There are various modes in which SAR can be operated in. Some include:

Stripmap SAR
In the stripmap mode in SAR, the direction of the radar antenna is held constant on the moving platform. A strip of the ground is formed as the beam points to the ground and thus an image is formed. The length of the strip is determined by length of the aperture, the height of the radar from ground, incidence angle of the radar and the illlumination time of the antenna. Fig. 1.2 shows an example of airborne SAR in stripmap case.
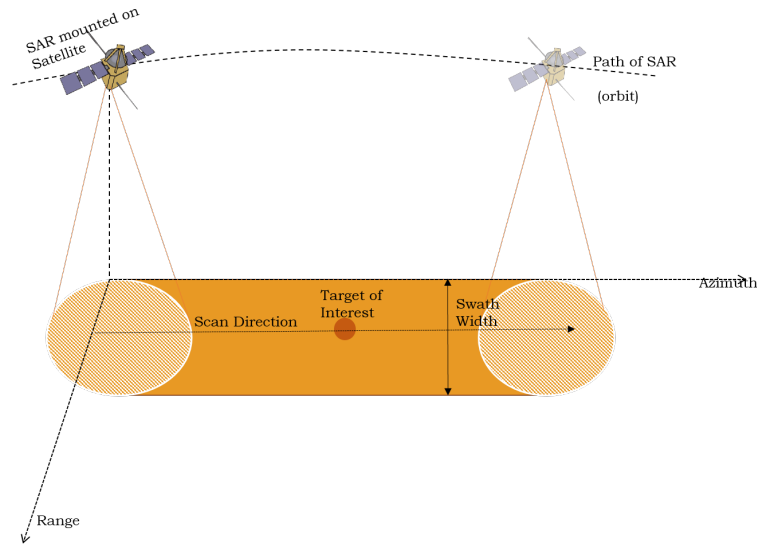
Figure 1.2: Stripmap SAR mode for a satellite acting as the transmitter and receiver.

Spotlight mode
In the spotlight mode, as shown in Fig. 1.3, a high resolution of the target of interest on ground is obtained by increasing the time and angle of illumination on the target. The radar beam is steered backwards when the radar sensor passes the scene. The steering of the antenna beam has a transient effect of simulating a wider antenna beam [1].The antenna is then steered forward and backwards towards the target of interest which increases the azimuth resolution but decreases the scene size.
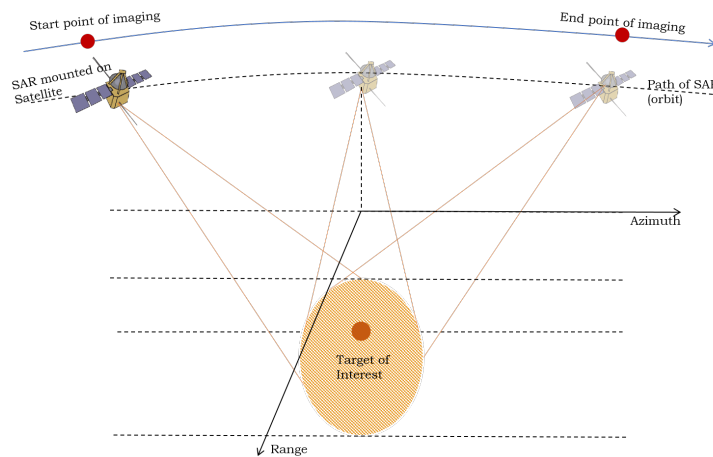
Figure 1.3: Spotlight SAR mode

Scan mode

Fig. 1.4 depicts the scan mode which is an extension to the Stripmap mode in SAR. This mode is an inverse concept of the spotlight mode. The antenna in this scenario makes several scans of the ground along the range direction resulting in a wider swath but a degraded azimuth resolution due to low azimuth bandwidth.
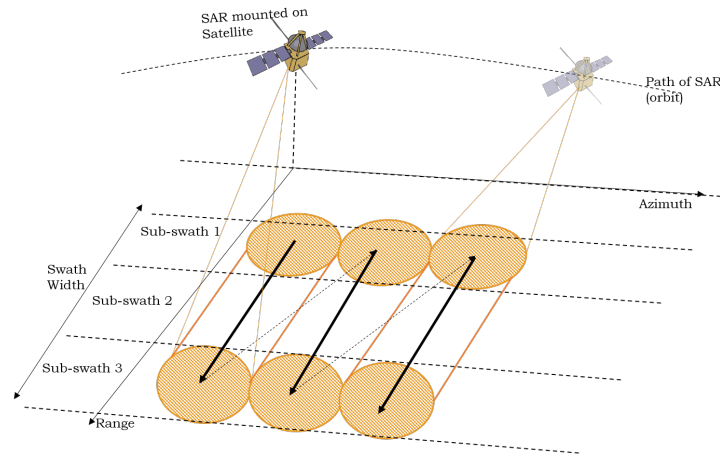
Figure 1.4: Scan SAR

Bistatic SAR

In this mode of SAR, the transmitter and receiver are placed separately at different positions as seen in Fig. 1.5. The transmitter transmits a number of pulses which are reflected back from the target of interest and are collected by the receiver. A bistatic or multistatic SAR system in airbone or spaceborne applications usually operate in a different platform or geometry and different co-ordinate systems. Hence such configurations normally may require accurate synchronization of time [3].
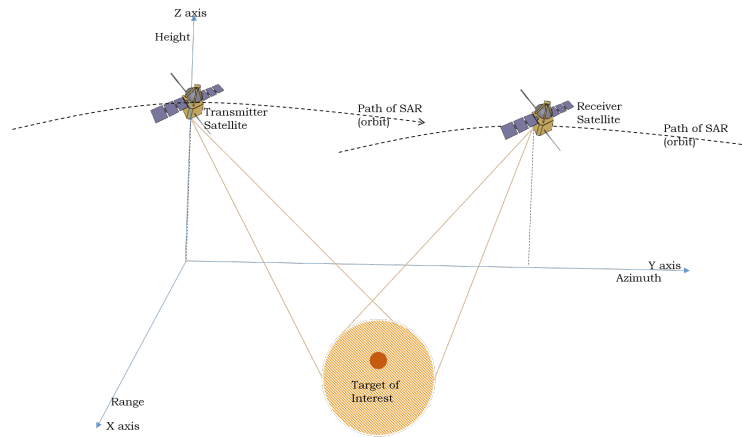
Figure 1.5: Bistatic SAR mode

1.2 BISTATIC SAR MISSIONS

The first experiments for bistatic SAR started in the mid-1970s at Stanford University and Scripps Institution of Oceanography to study ocean waves. The LORAN -A (LOng RAnge and Navigation) facility was used as a transmitter and the receiver was mounted onto a van and driven across roads, ramps and aircraft taxiways. The echoes from the ocean were processed coherently for a

long aperture of 0.8 to 2.7 km in order to achieve a good angular resolution[3]. A second experiment was conducted with a ship borne bistatic radar. The transmitter was placed on the mast of the ship and the receiver was separated at a distance of 25m and placed near the bow. The antennas pointed towards the surface of the ocean and the movement of the ship created a synthesized aperture of 350m measured for different frequency ranges.

Ten years later, an airborne bistatic SAR experiment was conducted by the Environmental Research Institute of Michigan [3]. Two air crafts with X-band SARs were flying in parallel trajectories measuring the target of interest at different bistatic angles. This eventually led to the knowledge on various issues such as the phase and time synchronization, antenna footprint matching and different bistatic focusing approaches.

Research on bistatic SAR has increased over the last decade and various experiments have been conducted on space-borne and airborne bistatic SAR by various countries. Some of the most notable ones are introduced as follows.

In November 2007, DLR (German Aerospace center) performed a spaceborne-airborne bistatic experiment with X- band SAR. TerraSAR-X was used as a transmitter and airborne F-SAR as a receiver. Trajectories of both platforms were designed to be nearly parallel to maximize footprint overlapping and to avoid poor range resolution configurations [3].
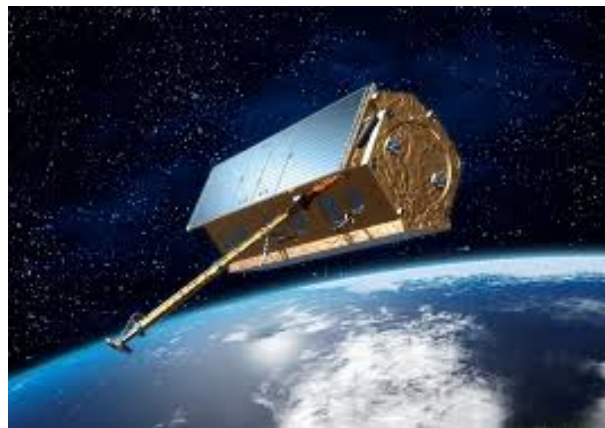
Figure 1.6: Depiction of TerraSAR-X [8]

Parameter	Values
Orbit	Sun synchronous
Mode	Stripmap
Antenna	Active Phased Array, Electronically beam steered
Antenna(azimuth)	$0.75°$
Antenna (elevation)	$20°$
Center frequency	9.56 GHz (X-band)
Chirp bandwidth	150 MHz/ 300MHz
Incidence Angle Range	$15°$-$60°$
TerraSAR-X velocity	7408 m/s
F-SAR velocity	90 m/s
TerraSAR-X altitude	514km
F-SAR altitude	2180 m

Table 1.1: TerraSAR-X and F-SAR parameters [8][9] [10]

Table 1.1 gives an overview of the specifications of TerraSAR-X. The transmitter, TerraSAR-X was operated in spotlight mode while the receiver, F-SAR in stripmap mode. The experiment was performed to overcome problems like synchronization but also gave rise to the understanding of different effects such as skewed target responses, the differences in brightness between monostatic and bistatic images. Various bistatic experiments similar to the DLR experiment were conducted. The first bistatic SAR formation in space is TanDEM-X which is closely similar to TerraSAR-X, Fig. 1.7. TanDEM-X and TerraSAR-X fly in close formation with a separation of 250m and 500m. The main objective of the mission is the generation of a consistent global digital elevation model with an unprecedented accuracy [4].
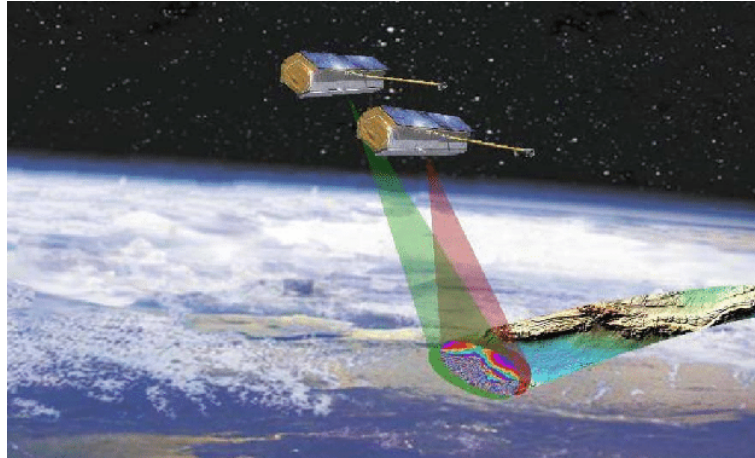
Figure 1.7: Depiction of TanDEM-X bistatic mission [11]

Parameter	Values
Orbit	Helix Orbit Type
Mode	Monostatic, bistatic or Alternating bistatic
Incidence Angle Range	20°-45° in Stripmap mode
Orbit height	514km at equator
Range Bandwidth	150MHz/ 300 MHz
Radar carrier frequency	9.65 GHz
TanDEM-X velocity	7.5km/s

Table 1.2: TanDEM-X parameters[12]

New techniques in digital beamforming with two satellites and single pass along track and polarimetric interferometry with different baseline configuration was explored in the TanDEM-X bistatic mission. Single pass L-band SAR interferometry was explored in the SAOCOM-CS mission which was a passive companion to the COSMO SkyMed, X-Band SAR. The mission was aimed to collect L-band SAR imagery with fully polarimetric and interferometric capabilities, for applications mainly in agriculture, forestry and hydrology [15]. The SEntinel-1 SAR Companion Multistatic Explorer (SESAME) is a passive SAR-satellite mission, comprising of two C-band SAR satellites flying in close formation to build a single pass interferometer [16]. The SESAME mission objectives are addressing applications in geoscience and climate research that require repeat measurements of high precision elevation data over land surfaces including ice covered areas and forests, and exploit the multistatic observation geometry of the satellite formation [16].
In 2018, a proposal for Stereo Thermo-optically Enhanced Radar for Earth, Ocean, Ice and land Dynamics(STEREOID) was accepted as a part of ESA's revolutionary satellite missions. The objective of the mission is to study and measure small shifts in glaciers and ocean surfaces. The mission aims and objectives are explained in detail in the following section.

1.3 INTRODUCTION TO STEREOID

The Stereo Thermo-optically Enhanced Radar for Earth, Ocean, Ice and land Dynamics (STEREOID) is one of the three candidates of the ESA Earth explorer 10 missions. It consists of 2 identical receive only spacecrafts and a Sentinel-1 C or D used as an illuminator. The novel constellation of STEREOID can provide flexible baseline configurations. The following figure gives an idea of the STEREOID configuration.
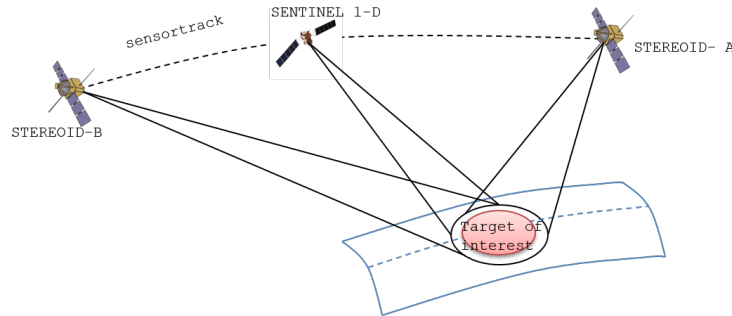
Figure 1.8: Configuration of STEREOID with an illuminator and two receivers separated at a distance of 250km

1.3.1 Objectives

1. The main objective of STEREOID mission is to provide high resolution data sets to study the deformation fields over ice sheets and glaciers.

2. It provides data for effective modeling and understanding of the sea dynamics.

3. STEREOID also provides 3D deformation fields related to seismic events, volcano and landslides. It also asses topographic changes over time due to volcano and landslides.

1.3.2 Characteristics of STEREOID

1. The spacecraft STEREOID A will fly at a distance of more than 250km from Sentinel-1 and STEREOID B will fly 250km behind Sentinel-1 on the same orbit.

2. The Sentinel-1 is used as an illuminator and consists of two small antennas spaced at a distance of 4.5m in flight direction. The antenna will utilize the phased array technology and digital beamforming which helps in acquiring improved scanning capabilities in elevation and full swath coverage for all modes of Sentinel-1.

1.3.3 Motivation and Problem Approach

The main goal of this thesis is to design an accurate and robust focusing strategy for STEREOID squinted illumination and evaluate the performance of STEREOID for different scenarios.
To achieve the goals,the following methods are approached.

1. A raw data simulator with a SAR imaging kernel is used. The kernel helps in image formation and focusing for different along track baseline bistatic configurations.

2. This is validated with point target simulations and extended for different bistatic geometries and bistatic TOPS acquisition mode.

3. TOPS acquisition mode is implemented and developed for different azimuth beamforming methods i.e., on-board and on-ground for single transmit and dual receive antennas.

4. The azimuth ambiguities, beam pointing errors and gain imbalances are evaluated for beamforming on ground and beamforming on-board.

2 | SAR SYSTEM AND DATA PROCESSING

2.1 INTRODUCTION TO SAR SYSTEM

A brief introduction to SAR and different SAR modes is given in Chapter 1. This section explains in detail, the SAR acquistion geometry. The following sections explain about the SAR data processing algorithms.

The SAR acquisition geometry for a spaceborne scenario is as shown in Fig. 2.1. A simple case of a monostatic synthetic aperture radar mounted on a satellite is assumed. The radar moves along an orbit at a constant velocity for a certain length when the target is illuminated. This length is the synthetic aperture length. When the platform moves, a number of electromagnetic pulses at sampled intervals are transmitted towards the target of interest on the ground. The radar antenna projects a beam on to the area surrounding the target on the ground, to illuminate the target. This is known as the beam footprint shown as a green patch in the Fig. 2.1. In SAR processing, the azimuth direction can be defined as the direction of the platform velocity of the sensor. When the sensor plane is almost perpendicular to the azimuth axis, this can be called as the zero Doppler plane. The slant range, R can be defined as the distance from the radar to the target. When the distance is minimum, R_0 is at zero Doppler and is known as the range of closest approach. The time of closest approach is the zero Doppler time. The projection of slant range, R onto the ground is the ground range. The ground range axis is orthogonal to the azimuth axis. This is mostly used to represent images in a maplike format. The squint angle, θ_{sq} is the angle made by the zero Doppler plane and the slant range vector [1].
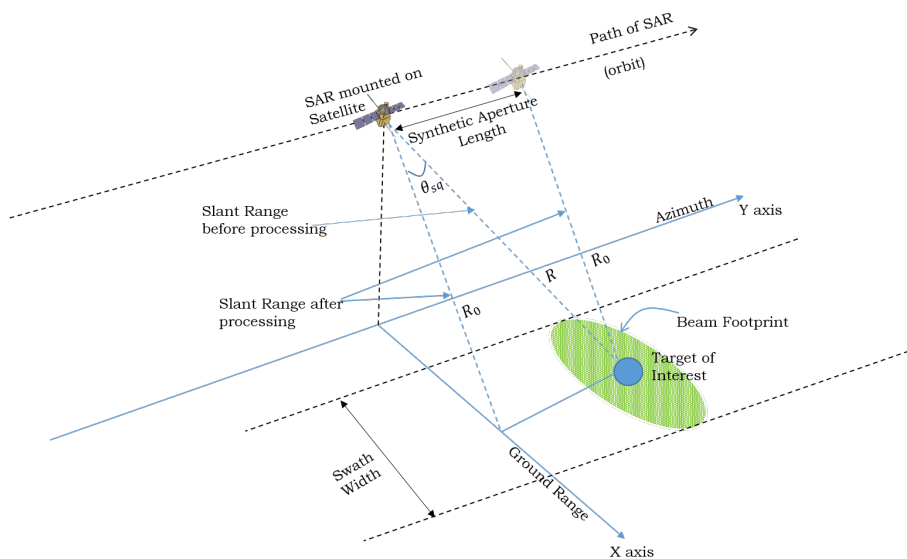
Figure 2.1: The SAR acquisition geometry for spaceborne SAR mounted on a satellite, illuminating a target of interest (blue dot) on the ground. The geometry assumed is for a stripmap mode.

2.2 SAR SIGNAL MEMORY

The SAR collects the received reflections from the scatterer and stores them in memory. The Fig. 2.2 shows that electromagnetic pulses are transmitted to the target of interest from the satellite at position 1. As the satellite advances in the orbit, it collects the received pulses and stores them in memory. At the end of position 2, the final signal is acquired from the target and stored.

Each signal received from the satellite is obtained with a constant time delay and is stored row-wise in the SAR signal memory. There is small movement of the satellite from one sample to the next along the azimuth time, η .Hence, it can be noted that the signals have been acquired in two directions namely, the range and azimuth direction. The range time is generally known as the "fast time" and is along the range direction and the azimuth time is generally known as the "slow time" which is along the azimuth direction. The signals are then processed with SAR signal processing algorithms to form a 2D image of the target.
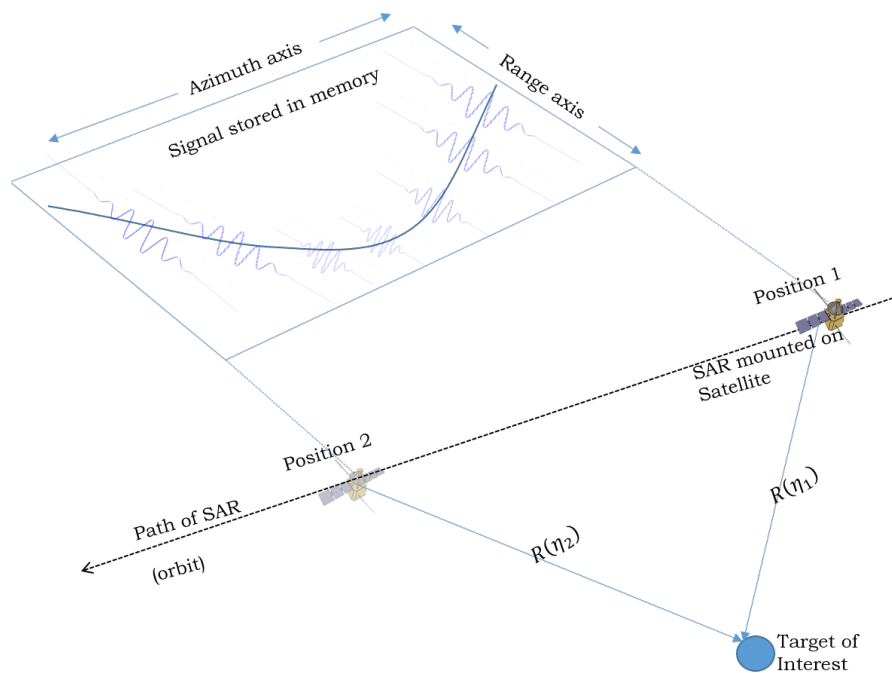
Figure 2.2: A depiction of the SAR signal memory. As the radar moves from position 1 at azimuth time η_1, it illuminates the target and stores the received echos in the signal memory. The signal is stored in a row and the samples are also stored along azimuth for the azimuth time, η. The echos are stored with a delay and at the end of position 2, η_2, the final signal is captured and stored. This results in the final two dimensional image in range and azimuth directions.

2.3 SAR DATA PROCESSING

There are various SAR processing algorithms in the time domain and frequency domain. The time domain algorithms help in phase preservation as they compensate the phases point by point. The time domain algorithms are robust and accurate but have high computational load due to the point by point image processing [13]. The frequency domain algorithms can improve block efficiency.

Some examples of time domain algorithms are Back Projection algorithm (BP) and Time Domain Correlation algorithm (TDC) [13]. The BP algorithm compensates phase of every point on the image and links it to the ground range coordinates without any need of additional steps [1]. The TDC algorithm match filters the baseband signal directly and the resultant is the perfect replica of

the echo signal. Hence, TDC helps in optimal reconstruction of the signal.

Some of the frequency domain algorithms are the Range-Doppler algorithm (RD), $\omega - k$ algorithm and chirp scaling algorithm [13]. The Range-Doppler Algorithm is the first and most widely used algorithm for SAR processing of Satellite Data because of its efficiency, accuracy, maturity and ease of implementation [1]. The Range Doppler algorithm (RD) allows for efficient block processing in frequency domain for range and azimuth. The processing occurs in separate directions with large time scale difference in the range and azimuth direction using range cell migration correction (RCMC). The RCMC operation is performed in range time and azimuth frequency domain, hence the name "Range-Doppler" algorithm. The key features of RDA is it allows efficient and simplified processing of one dimensional arrays. The chirp scaling algorithm focuses on two dimensional frequency domain processing and eliminates the use of RCMC with a much more accurate phase compensation technique. This algorithm transforms the 2D frequency domain data back to Range-Doppler domain and this may not be suitable for wide apertures and high squint angles. The $\omega - k$ algorithm overcomes this disadvantage by correcting the range and azimuth dependence [1]. Hence the $\omega - k$ algorithm can process for high squint angles and wide apertures. The following section explains the Range-Doppler algorithm. This algorithm is studied and explored to give an overview of SAR processing.

2.4 RANGE–DOPPLER ALGORITHM

A flowchart of the Range-Doppler Algorithm is depicted in, Fig. 2.3 to support the different stages involved in the algorithm.
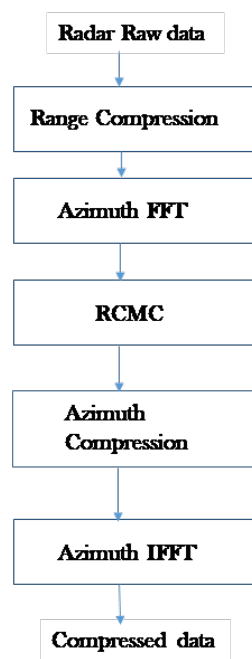
Figure 2.3: Flowchart of the Range-Doppler Imaging Algorithm

2.4.1 SAR Signal Model

The data received from the SAR system is the raw data and is demodulated to baseband signal. This section elaborates on the signal modelling of the raw data. The transmit signal is generated by a simple Linear Frequency Modulated (LFM) waveform given by

$$r_x(t) = e^{(j2\pi f_0 t + \pi \alpha t^2)},$$ (2.1)

where, f_0 is the center frequency, α is the chirp rate given by $\alpha = \frac{Bandwidth}{Chirp\ duration}$, t is the chirp interval, $-m\ f_i \leq t \leq m\ f_i$ and f_i is the fast time sampling interval and m is the fast time samples.

The received signal is given LFM with a parabolic phase delay known as the Doppler history caused due to the sensor position and change of distance between the sensor and the target along the slow time. Hence the demodulated echo data whose center range frequency is zero, is expressed as a function of range time and azimuth as,

$$r_y(t, \eta) = rect(t_1 - t_d(\eta)\ e^{\{j\pi\alpha(t_1 - t_d(\eta))^2\}} e^{\{-j2\pi f_0 t_d(\eta)\}},$$ (2.2)

where, η is the slow time ranging between, $-k\ PRI \leq \eta \leq k\ PRI$, PRI is the pulse repetition interval or the slow time sampling interval, and k is the slow time samples.
$t_d(\eta) = \frac{2R(\eta)}{c}$, the Doppler history as a function of slow time, $R(\eta) = \sqrt{(R_0 + V_r^2 \eta^2)}$, azimuth range as a function of zero Doppler slant range R_0, satellite velocity V_r and slow time. t_1 is the fast time interval of received chirp. t_1 ranges between $-m\ f_i + \tau_c \leq t_1 \leq m\ f_i + \tau_c$ and $\tau_c = \frac{2R_0}{c}$.

2.4.2 Range Compression

The transmitted and the received signal is range compressed by the process of matched filtering in range frequency domain.The transmitted signal given by $r_x(t)$, in frequency domain is, $r_x(f)$. The received signal in time domain is given by $r_y(t, \eta)$, in frequency domain is $r_y(f, \eta)$. Hence the output of the range matched filter is given by,

$$s_{mf}(t, \eta) = IFFT\left\{r_y(f, \eta)\ r_x(f)\right\}.$$ (2.3)

The rectangular window function becomes a sinc function with sidelobes. The functions dependent on range have sinc-like range envelope and the functions dependent on azimuth remain unaffected.

2.4.3 Azimuth Fourier Transform

The next stage in processing is to take an azimuth FFT of Eqn. 2.3. This transforms the data to range-Doppler domain. Therefore,

$$S_{az}(t, f_\eta) = FFT\left\{s_{mf}(t,\ \eta)\right\}.$$ (2.4)

The functions dependent on azimuth carry phase information , important for applications such as interferometry and polarimetry but do not play a role in the intensity of the image [1].

2.4.4 Range Cell Migration Correction

RCMC is a technique which is used to correct the Range Cell Migration (RCM). RCM is the instantaneous change of the slant range with azimuth time and can be expressed as a hyperbolic function. The target trajectory migrates through different range cells which is one of the key features of SAR. This component is expanded in power series as,

$$R(\eta) = R_0 + \frac{V_r^2 \eta_c}{R_0}(\eta - \eta_c) + \frac{1}{2}\frac{V_r^2 \cos^2 \theta_{r,c}}{R_0}(\eta - \eta_c)^2 + \ldots \qquad,$$ (2.5)

where, $R(\eta)$ is the range history, η_c is the beam centre offset time, $\theta_{r,c}$ is the squint angle. The higher order terms in the range history equation are usually ignored because they are comparatively small to the range cell size. The RCM component in the frequency domain is given by,

$$R\left(f_{\eta}\right) = R_0 + \frac{V_r^2}{2R_0}\left(\frac{f_{\eta}}{K_a}\right)^2, \tag{2.6}$$

where, $K_a = \frac{2V_r^2}{\lambda R_0}$ is the linear FM rate. In order to correct the effect of RCM, two approaches are suggested. The first method is to implement a RCMC interpolator which is usually a sinc interpolator designed based on the shift quantization, kernel length and the coefficient values of the window [1]. Another method of implementation is to use a phase multiplier using an FFT linear phase multiplication and an IFFT technique. The amount RCM required for correction is given by,

$$\Delta R\left(f_{\eta}\right) = \frac{\lambda^2 R_0 f_{\eta}^2}{8V_r^2}, \tag{2.7}$$

The phase multiplied and compensated with the following equation,

$$p_{rcmc}\left(f_t\right) = \exp\left\{j\frac{4\pi f_t \Delta R\left(f_{\eta}\right)}{c}\right\}. \tag{2.8}$$

2.4.5   Azimuth Compression and Azimuth Inverse Fourier Transform

The next stage after Range Cell Migration Correction is to apply a matched filter to the obtained data in the azimuth direction. The data is multiplied by a frequency domain matched filter given by,

$$M_{az}(f_{\eta}) = \exp\left\{-\frac{j\pi f_{\eta}^2}{K_a}\right\}, \tag{2.9}$$

The azimuth compressed result can be expressed as,

$$S_{ac}\left(t, f_{\eta}\right) = S_{rcmc}\left(t,\ f_{\eta}\right) \cdot M_{az}\left(f_{\eta}\right). \tag{2.10}$$

IFFT of the above equation results in the final SAR image of a point target given by,

$$S_{final}\left(t, \eta\right) = IFFT\left\{\left(t,\ f_{\eta}\right)\right\}. \tag{2.11}$$

2.5   PARAMETERS FOR PERFORMANCE ANALYSIS

The parameters considered for performance analysis of targets for most SAR processing algorithms is Resolution, Peak to Side Lobe Ratio (PSLR) and Integrated Side Lobe Ratio (ISLR) in both range and azimuth directions.

Resolution: This parameter is considered as the -3dB width across mainlobe and is governed by the bandwidth of the pulse. The resolution across range is given by the following equation,

$$R = \frac{c}{2B}, \tag{2.12}$$

where, c is the speed of light and B is the bandwidth of the pulse.
In azimuth direction, the resolution is given by,

$$\rho_a = \frac{0.886\lambda}{2L_a}, \tag{2.13}$$

where, L_a is the synthetic aperture length of the radar.

Peak to Side Lobe Ratio (PSLR): Peak to Sidelobe Ratio is defined as the ratio of the peak intensity of highest level of sidelobes (I_s) to the peak intensity of the mainlobe level (I_m) (ref. Eqn. 2.14). The ideal value of PSLR is given by -13.26 dB PSLR indicates the ability of the radar to distinguish a strong target over a weak one, without the use of windowing techniques.

$$PSLR = 10log_{10}(\frac{I_s}{I_m}).$$ (2.14)

Integrated Side Lobe Ratio (ISLR): *is the ratio of energy power in the mainlobe to the total energy power in the sidelobes.* A general sidelobe ratio determines the ability of the radar to detect two targets with two different amplitude levels. But an ISLR evaluates the ability of radar to determine the presence of multiple targets. The typical value of ISLR is given by -9.7 dB without the use of widows, and this can be expressed as,

$$ISLR = 10 \log_{10} \frac{\int_{-\infty}^{a} |x(t)|^2 \ dt \ + \ \int_{b}^{\infty} |x(t)|^2 \ dt}{\int_{a}^{b} |x(t)|^2 \ dt},$$ (2.15)

where, $x(t)$ is the signal for which ISLR is to be measured. a, b are the null points of the mainlobe. The above mentioned parameters are used to evaluate RD and BP algorithms implemented in this thesis.

2.6 SIMULATION RESULTS AND PERFORMANCE ANALYSIS

The evaluation was performed for a zero Doppler,monostatic broadside looking spaceborne SAR with a height of 250 km from ground and a ground range of 1 km. The target was assumed to be at origin. The following Table 3.1 provides the parameters, considered [1] for the simulation results (ref. Fig. 2.4) and the performance analysis.

Parameter	Values
Bandwidth	100 MHz
Chirp duration	8μ sec
PRF	10 KHz
Ground range	1 km
Height	250km
Target (x, y)	(0 m, 0 m)
Synthetic Aperture Length	1 km
Effective Radar Velocity	7100 m/s
Beam Footprint velocity	7000m/s

Table 2.1: Parameters considered for the simulation of the following results

(a)

(b)

(c)

(d)
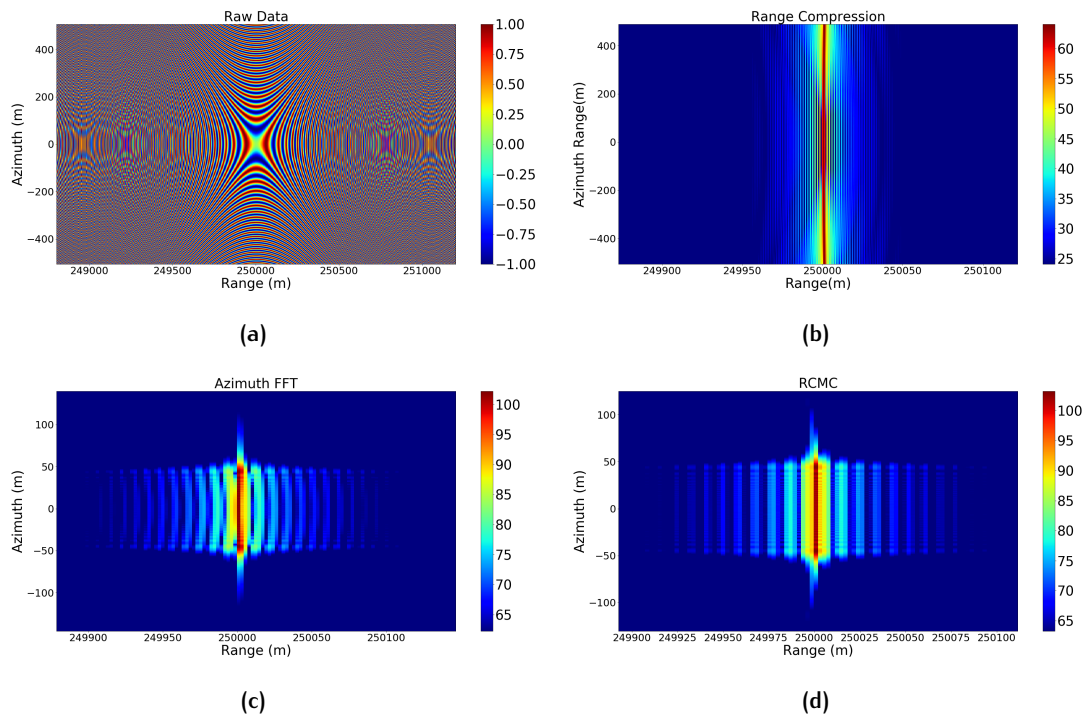
Figure 2.4: Simulated results of single point target for given parameters. Fig.(a) shows the real part of the complex signal of the Raw Data for a Zero Squint Case. Fig.(b) is the range compressed result of raw data and a parabolic phase can be observed. The data is spread across many range cells. Fig.(c) depicts the result of azimuth Fourier Transform of the range compressed data and hence transforms the result to the "Range-Doppler" domain. Fig.(d) represents the data after the range cell migration correction. The phase has been compensated using a phase multiplier. For all cases the point target lies at a slant range, R_0 of approx. 250km for the given parameters.
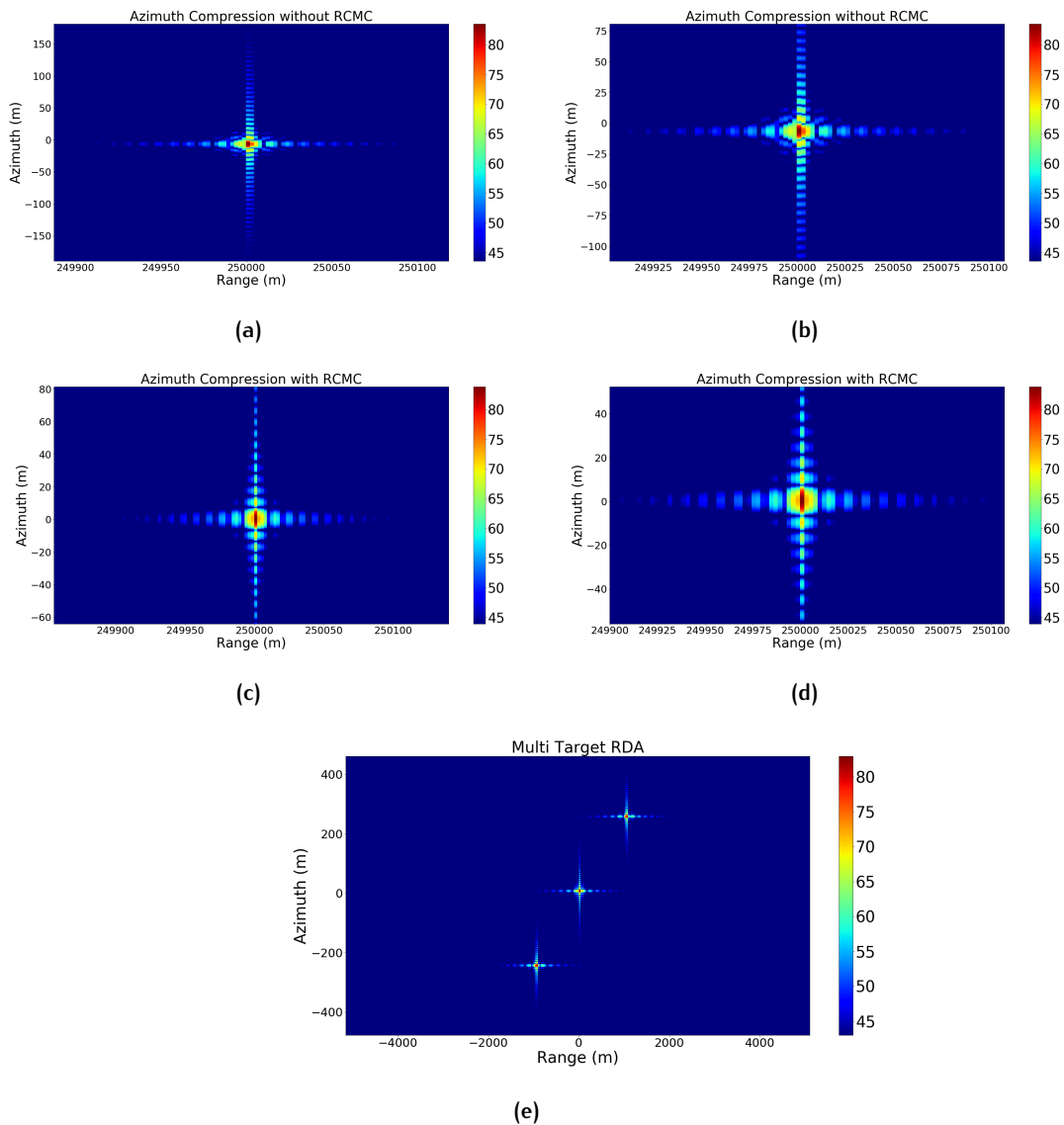
Figure 2.5: Fig.(a) represents the point target without range cell migration correction and Fig.(b) shows a magnified version of Fig.(a). It is observed that if the migration is not corrected then a broadening of the impulse response occurs in both range and azimuth directions. Fig.(c) and Fig.(d) represent the point target at R_0 of approx. 250km and azimuth range of approx. 0m after RCMC. Fig.(e) represents the application of RD algorithm for multi target scenario for targets placed at a range of -1km, 0 km and 1km for an azimuth range of 250m, 0m and -250m.

The simulation results for a single and multiple point targets is depicted in Fig. 2.4 and Fig. 2.5. In Fig. 2.4 (a), the raw data of the real part of complex signal is depicted. The case is simulated for a zero squint and only a part of the data is represented. Hence the phase of up chirped data is the same as the real part of the raw data [1]. In Fig. 2.4 (b), the range compressed data is spread across many range cells in time domain for a slant range of R_0 of 250km. Fig. 2.4 (c) depicts the data in "Range-Doppler" domain. The parabolic phase history in time domain and range Doppler domain is that the curvature of the phase history decreases with range in the time domain and increases with range in the frequency domain. The width of the phase history is observed to decrease in the range- Doppler domain when compared to the range–azimuth time figure. This occurs due to the PRF as it depends on the azimuth sampling rate. If the PRF is decreased then there would be an

overlap of the samples in the azimuth domain as the number of samples in slow-time depends on PRF and can be expressed as,

$$N_{slow\ time} = \frac{La}{V_g} PRF, \tag{2.16}$$

where, La is the synthetic aperture length and V_g is the beam foot print velocity. Fig. 2.4 (d) represents the corrected migration of range cells using the phase multiplication method. The RCM mainly occurs due to migration of trajectories across various range cells when stored in signal memory as previously depicted in Fig. 2.2. The main feature of RCM is that it represents the variation of slant range with time that imposes an FM characteristic on the signal in the azimuth domain [1]. The effect of RCM without correction can further be seen in Fig. 2.5 (a), (b).The uncorrected range cell migration causes a broadening of the impulse response width in both azimuth and range. The broadening effect in range is due to the off-centered range compressed data as the operation of compression across azimuth is effectively performed. Similarly, the broadening effect across azimuth can be explained due to the loss of azimuth bandwidth which exists in a single range cell. The azimuth is smeared across multiple range cells which in turn reduces the bandwidth in the area where the target energy has to be captured. Hence the correction is necessary and the results can be observed in Fig. 2.5 (c), (d). The point target can be observed at a slant range R_0 and azimuth range of approximately 250 km and 0 km respectively. The algorithm was further extended to multiple targets placed at different range and azimuth directions. The performance analysis of single and multi-target scenario is explored in the following sections.

2.6.1 Performance analysis for a Single Target

A range and azimuth cut has been performed across both directions of the point target indicated as in Fig. 2.6. The process is followed for targets placed at different range and azimuth directions.
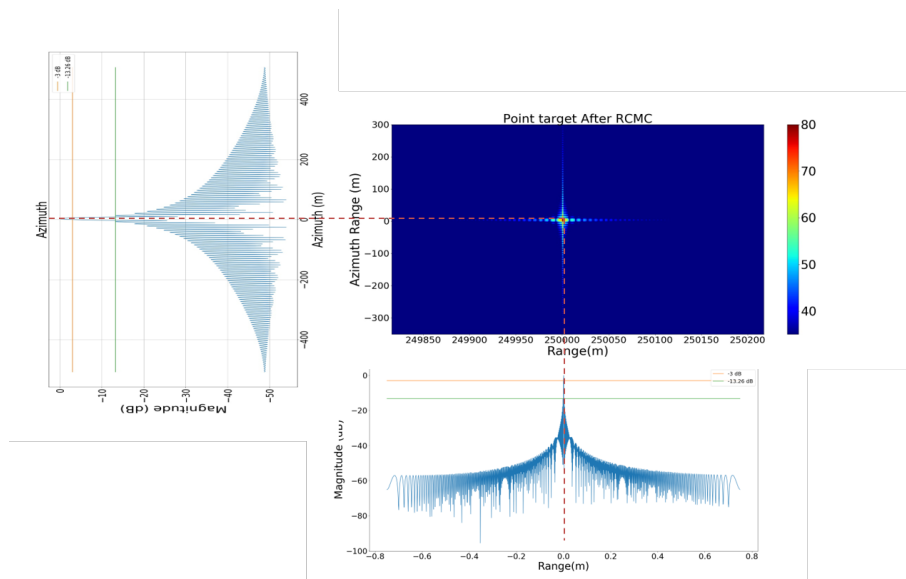
Figure 2.6: Range and azimuth cut of the point Target to evaluate parameters such as resolution, PSLR and ISLR. The same process also follows for the multi-target scenario.

(a)   (b)
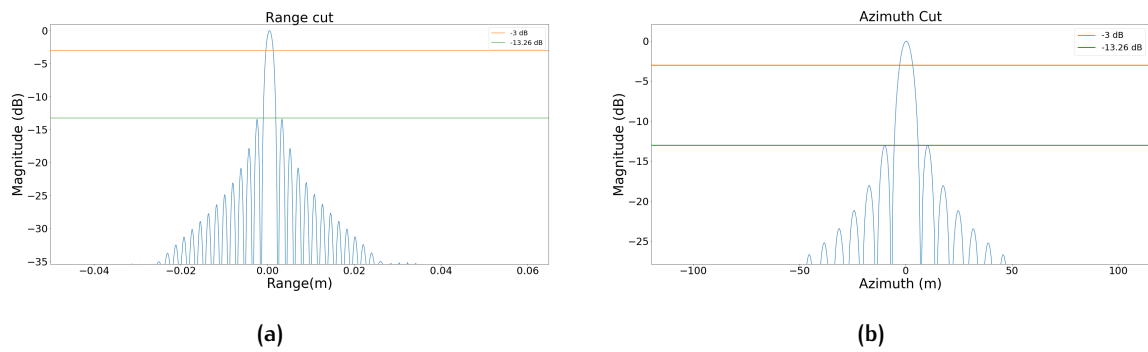
Figure 2.7: Range and Azimuth cut of the point target at a slant range of 250km and azimuth range of 0m respectively. The -3dB line represents the evaluation of resolution of target across both range and azimuth directions. The -13.26 dB is for the evaluation of PSLR in both directions.

The values evaluated for the performance analysis of single target is given in Table 2.2

Parameter	Direction	Theoretical	Practical
Resolution(m)	Range	1.49	1.88
Resolution(m)	Azimuth	6.26	6.38
PSLR (dB)	Range	-13.26	-13.73
PSLR (dB)	Azimuth	-13.26	-13.30
ISLR (dB)	Range	-9.7	-9.03
ISLR (dB)	Azimuth	-9.7	-9.54

Table 2.2: Performance analysis for single target

The 3-dB resolution for single target located at (0m, 0m) was evaluated along range and azimuth. The theoretical values are almost equal to the practical values for all metrics. The influence of sidelobes on the mainlobe is almost equal to the ideal value.

2.7 PERFORMANCE ANALYSIS FOR MULTIPLE TARGETS

The following table 2.3 are the parameters considered for multiple targets.

Parameter	Values
Bandwidth	100 MHz
Chirp duration	8μ sec
PRF	10 Khz
Ground Range	10km
Height	500 km
Synthetic Aperture Length	1 km
Target1 (x, y)	$(1 \times 10^3$ m, 250 m)
Target2 (x, y)	(0 m, 0 m)
Target3 (x, y)	$(-1 \times 10^3$ m, -250 m)
Effective Radar Velocity	7100 m/s
Beam Footprint velocity	7000m/s

Table 2.3: Parameters considered for the simulation of multiple targets placed at different range and azimuth directions.

The performance analysis for the multiple targets is given below in Table 2.4. The theoretical range resolution is 1.49m and azimuth resolution is 6.26m. This was evaluated using the equations

2.12 and 2.13. It can be seen that the practical values of analysis is almost close to that of the theoretical value. The influence of sidelobes with respect to the main lobe is comparatively close to the ideal value.

Parameter	Direction	Theoretical	Practical
Target (1×10^3 m, 250 m)			
Resolution(m)	Range	1.49	1.99
Resolution(m)	Azimuth	6.26	6.38
PSLR (dB)	Range	-13.26	-13.27
PSLR (dB)	Azimuth	-13.26	-13.21
ISLR (dB)	Range	-9.7	-9.03
ISLR (dB)	Azimuth	-9.7	-9.54
Target (0 m, 0 m)			
Resolution(m)	Range	1.49	1.99
Resolution(m)	Azimuth	6.26	6.39
PSLR (dB)	Range	-13.26	-13.27
PSLR (dB)	Azimuth	-13.26	-13.24
ISLR (dB)	Range	-9.7	-9.03
ISLR (dB)	Azimuth	-9.7	-9.54
Target (-1×10^3 m, -250 m)			
Resolution(m)	Range	1.49	1.91
Resolution(m)	Azimuth	6.26	6.38
PSLR (dB)	Range	-13.26	-13.28
PSLR (dB)	Azimuth	-13.26	-13.25
ISLR (dB)	Range	-9.7	-9.03
ISLR (dB)	Azimuth	-9.7	-9.54

Table 2.4: Perfomance analysis for multi-target scenario

From the above table evaluated for multiple targets placed at (1 km, 250m), (0m , 0m) and (-1km, -250m), it can be observed that the theoretical resolution value is close to practical value. This indicates that the multiple targets placed along both range and azimuth are distinguishable. The influence of sidelobes is determined by ISLR and PSLR. It can be observed that the values are close to theoretical values which indicate that there is an independent strong detection of multiple targets. The most important feature of the RD algorithm is the correction of one phase history corrects a group of phase histories for multiple targets and can be observed in Fig. 2.5(e).Hence the Range-Doppler algorithm is efficient, accurate and can be implemented easily.

2.8 CONCLUSION

This chapter explores some of the basic concepts of SAR , SAR signal memory and a simple algorithm of SAR imaging, the Range-Doppler algorithm. The algorithm was evaluated and studied for single and multiple targets to understand the concept behind imaging in SAR. The thesis focuses on Backprojection algorithm for evaluation of the bistatic scenario in STEREOID.

3 | BISTATIC SAR SYSTEM AND DATA PROCESSING

3.1 BISTATIC SAR SYSTEM

Bistatic Synthetic Aperture Radar(SAR) is a distributed observation system based on a separate transmission and reception of frequency modulated signals [3]. The configuration consists of a transmitter and receiver systems separated at a distance, illuminate a target of interest on the ground. The bistatic system demands precise antenna pointing and time synchronization between transmitter and receiver antennas, which helps the system realize a flexible baseline configuration.

3.1.1 Bistatic Geometry

The main constituents of the bistatic system are the transmitter, receiver and the target of interest on the ground (ref. Fig. 3.1). The transmitter and receiver are separated by a distance known as the along track baseline separation. The transmitter transmits a number of pulses towards the target, the pulses are partly scattered and reflected back to the receiver. The data is collected and stored as a two dimensional image along slow time and fast time, discussed in Chapter 2. The SAR signal memory can easily be explained in terms of range and azimuth for a monostatic case. For a bistatic case, this definition may not strictly hold as the positions and velocities of each satellite may vary.
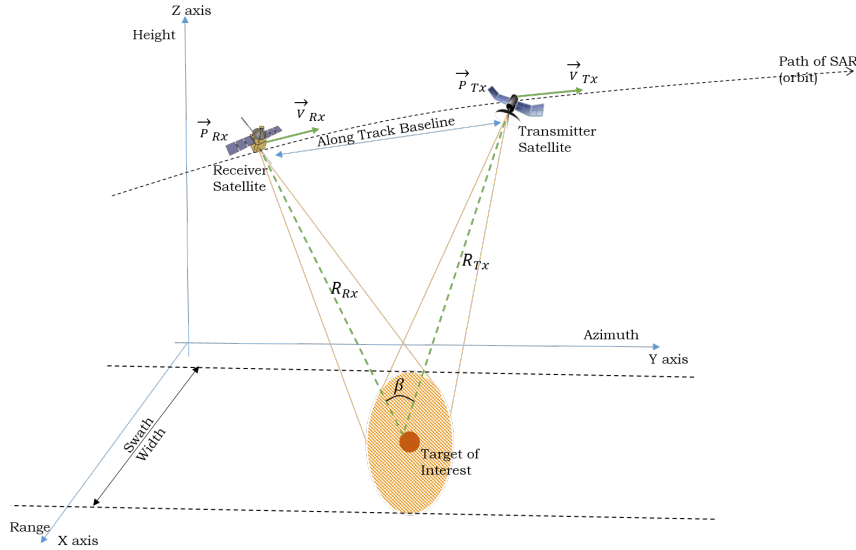
Figure 3.1: Depiction of bistatic geometry. The transmitter satellite and receiver satellite have position vectors, $\vec{P_{tx}}$ and $\vec{P_{Rx}}$ respectively, and velocity vectors, $\vec{V_{tx}}$ and $\vec{V_{Rx}}$ respectively. The transmitter satellite illuminates the target on ground and the receiver collects the reflected pulses and stores in memory. The slant range axis of transmitter, R_{Tx} and receiver, R_{Rx} form a bistatic angle, β. The transmitter and receiver are separated by a distance known as the along track baseline.

The geometry of bistatic SAR can vary for different scenarios. Generally, the bistatic synthetic aperture can be obtained from the relative position of transmitter and receiver, $\vec{P_{Tx}}$ and $\vec{P_{Rx}}$ respectively, relative motion of the satellite, $\vec{V_{Tx}}$ and $\vec{V_{Rx}}$ respectively, the slant range of both satellites,

R_{Tx} and R_{Rx} respectively. The target of interest is assumed to be stationary. A more demanding bistatic SAR configuration can involve multiple transmitters and/or multiple receivers, MIMO (Multiple Input Multiple Output) SAR can also be envisaged with monostatic or non monostatic transmitters [3].

3.1.2 Bistatic Resolution Analysis

The resolution analysis for a monostatic case was explained in Chapter 2 with Eqn. 2.12 and Eqn. 2.13. It can be noted that in the monostatic case, the evaluation of resolution is easier as the range and Doppler resolutions are orthogonal to each other. This approach does not apply for the bistatic case as the position of transmitter and receiver is arbitary, the range and azimuth resolutions, in bistatic case, are not orthogonal leading to range-azimuth coupling. Hence, the evaluation of resolution is performed through the gradient method . The key point in such a system is that the azimuth and range directions do not strictly exist and image pixels are interpreted by intersecting iso-time delay and iso-Doppler lines [3].

The range resolution can be defined as the change in round trip delay when a pulse is transmitted and reflected back from a target of interest. Similarly, the Doppler resolution can be defined as the instantaneous range from the transmitter to a target of interest and back to the receiver for a given time. The direction of the gradient time delay indicates the direction of best fast time resolution as it is the direction that maximises the change in time delay , t along the projection of time $\vec{\nabla}t$ on the local horizontal plane $\vec{\nabla}t_g$ and minimizes the resolution along range. Similarly, the direction of gradient Doppler identifies the best Doppler resolution, since the change in Doppler frequency, ∇f is maximum along the projection of frequency $\vec{\nabla}f$ on the local horizontal plane $\vec{\nabla}f_g$. Therefore for the bistatic scenario, the geometric resolution is computed which deals with the separation of two targets with same amplitude in one or more dimensions [3]. The geometric resolution depends on parameters such as the integration time, bandwidth and acquisition geometry. The following equations for geometric range and Doppler resolutions are given for arbitary bistatic SAR geometry configurations. The ground range resolution can be expressed as,

$$\Delta\vec{r}_g = \frac{1}{BW|\vec{\nabla}t_g|}\vec{i}_{t_g},$$ (3.1)

where, BW is the bandwidth, $\vec{\nabla}t_g$ indicates the ground projection of gradient time delay, $\vec{i}_{t_g}$ is the unit vector along the direction of $\vec{\nabla}t_g$. The gradient of time delay is given by $\vec{\nabla}t$ is given by the equation,

$$\vec{\nabla}t = \frac{1}{c}\left(\frac{\vec{R}_{Tx}}{R_{Tx}} + \frac{\vec{R}_{Rx}}{R_{Rx}}\right) = \frac{1}{c}(\vec{i}_{Tx} + \vec{i}_{Rx}),$$

(3.2)

$$\vec{R}_{Tx} = \vec{P}_{Tx} - \vec{r}$$
$$and$$
$$\vec{R}_{Rx} = \vec{P}_{Rx} - \vec{r},$$

where, $\vec{R}_{Tx}$ and $\vec{R}_{Rx}$ is the slant range vector, $\vec{P}_{Tx}$ and $\vec{P}_{Rx}$ are the position vectors of transmitter and receiver satellites respectively. $\vec{r}$ is the target range. The ground range resolution can also be expressed in terms of incidence and transmitter out of plane angles as follows:

$$\Delta\vec{r}_g = \frac{c}{BW\sqrt{sin^2\theta_{Tx} + sin^2\theta_{Rx} + 2\,sin\theta_{Tx}\,sin\theta_{Rx}\,cos\phi}}\vec{i}_{t_g},$$ (3.3)

$\vec{i_{tg}}$ can be expressed as,

$$\vec{i_{tg}} = \begin{bmatrix} \dfrac{sin\theta_{Tx}\ cos\phi + sin\theta_{Rx}}{\sqrt{sin^2\theta_{Tx} + sin^2\theta_{Rx} + 2\ sin\theta_{Tx}\ sin\theta_{Rx}\ cos\phi}} \\[4mm] \dfrac{sin\theta_{Tx}\ sin\phi}{\sqrt{sin^2\theta_{Tx} + sin^2\theta_{Rx} + 2\ sin\theta_{Tx}\ sin\theta_{Rx}\ cos\phi}} \end{bmatrix}, \tag{3.4}$$

where, c is the speed of light, θ_{Tx} is the incidence angle of transmitter, θ_{Rx} is the incidence angle of the receiver, ϕ is the transmitter out of plane angle as depicted in Fig. 3.2 and i_{tg} is vector perpendicular to the Iso-range lines.
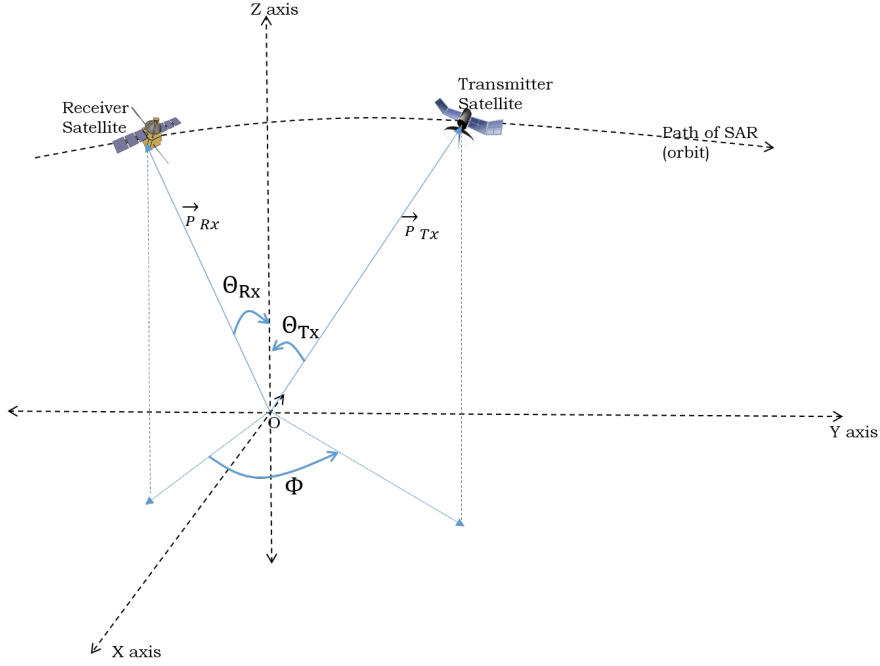
Figure 3.2: The incidence angles and out of plane angles are shown in the figure for the target located at origin. The incidence angle of the transmitter and receiver,θ_{Tx} and θ_{Rx} is the angle made by the position vectors with respect to the origin.The out of plane angle, ϕ is the angle made by the projection of position vectors onto the ground with respect to the origin.

The ability to distinguish targets in the slow time is given by the Doppler resolution expressed as,

$$\vec{\bigtriangledown}a = \frac{1}{T|\vec{\bigtriangledown}f_g|}\vec{i_{fg}}, \tag{3.5}$$

where, T is the integration time or synthetic aperture duration, $\vec{\Delta f_g}$ is the ground projection of gradient Doppler frequency and $\vec{i_{fg}}$ is the unit vector perpendicular to the iso-Doppler lines. The projection of Doppler frequency,$\vec{\bigtriangledown}f$, can be given by the equation,

$$\vec{\bigtriangledown}f = \frac{1}{\lambda}\left(\frac{1}{R_{Tx}}(\vec{V_{Tx}} - (\vec{V_{Tx}} \cdot \vec{i_{Tx}}))\vec{i_{Tx}} + \frac{1}{R_{Rx}}(\vec{V_{Rx}} - (\vec{V_{Rx}} \cdot \vec{i_{Rx}}))\vec{i_{Rx}} \right), \tag{3.6}$$

where, $\vec{V_{Tx}}$ and $\vec{V_{Rx}}$ are the velocity vectors of the transmitter and receiver satellites. The above equation is then projected on to the local horizontal plane to obtain the ground projection of Doppler frequency, $\vec{\bigtriangledown}f_g$.

Iso-Range and Iso-Doppler Lines

The Iso-Range lines are concentric circles formed on the Earth's surface with its centre at the nadir point of the sensor. The nadir point is a point on the Earth's surface below the sensor such that

the normal to Earth's surface passes through the sensor. The Iso-Doppler lines are formed with the cuts of the Doppler cone with respect to the Earth's surface. The Doppler cone has its vertex located at the phase center of the antenna and its axis in the direction of flight. The formation of the lines are depicted in Fig. 3.3.
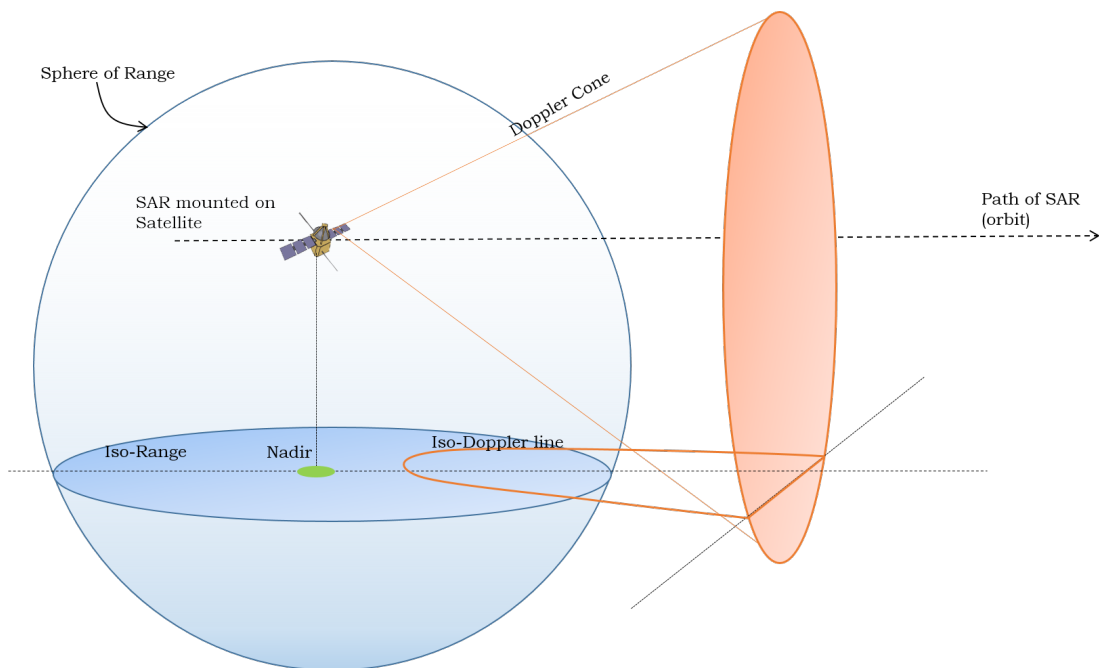
Figure 3.3: Depiction of the formation of Iso Range and Iso Doppler Lines from the Range Sphere and Doppler cone respectively. The Iso-range and Iso-Doppler lines indicate the constant time delay and Doppler shift respectively.

3.2 BISTATIC SAR DATA PROCESSING

In Chapter 2, a few notable time domain and frequency domain algorithms were discussed. The time domain Back projection algorithm was chosen among them, for its accuracy, robustness for different geometrical configurations. The following sections explain about the application of BP for bistatic SAR processing with simulations and performance analysis. The general flowchart of the back projection algorithm is depicted in the Fig. 3.4.
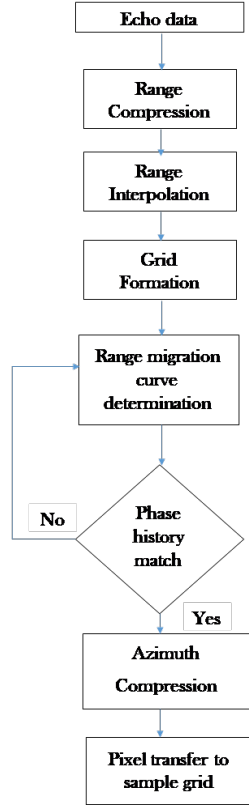
Figure 3.4: Flowchart of the Back Projection Algorithm

Echo data Generation and Range Compression

The raw data generation and range compression follows the same process explained in Range Doppler Algorithm of Chapter 2. Hence the Eqn. 2.2 and Eqn. 2.3 hold for Back Projection algorithm as well.

Range Interpolation

The following step of the BP algorithm is the range interpolation, obtained by zero padding of the range compressed data in the range domain. Zero padding helps increase the number of samples in the range domain and thus the phase or Doppler history can easily and accurately be traced. Zero Padded data can be expressed as,

$$
s_{intp}(t,\eta) = \begin{bmatrix} s_{mf}(t_1,\eta_1) & s_{mf}(t_1,\eta_2) & s_{mf}(t_1,\eta_3) & \dots & \dots & 0 & 0 & 0 \\ s_{mf}(t_2,\eta_1) & s_{mf}(t_2,\eta_2) & s_{mf}(t_2,\eta_3) & \dots & \dots & 0 & 0 & 0 \\ \vdots & \vdots & \vdots & \dots & \dots & 0 & 0 & 0 \\ \vdots & \vdots & \vdots & \dots & \dots & 0 & 0 & 0 \end{bmatrix}, \tag{3.7}
$$

where, s_{intp} is the interpolated matrix and s_{mf} is the matched filtered data. The number of zeros to be padded are calculated as $2^{2n} \cdot N_f$ to make the FFT operation faster where, N_f is the number of fast time samples.

Grid Formation

In this step, a sample grid is formed of the imaging scene where each cell of the grid is finer than that of the theoretical range and azimuth resolution. This is achieved by dividing the total

scene length on each axis by the grid interval. This empty grid is then translated to the geodetic co-ordinates with the x axis constituting the latitude and y axis representing the longitude.

Determination of the Phase History

Every cell in the sample grid consists of a phase history which is compared against the phase history of the of the range interpolated data at every range. When a close match between the phase history and the range interpolated data occurs, the curve is extracted. The following Fig. 3.5 gives a pictorial representation the extracted the data respectively which had a match with the phase history in the cells of the grid.
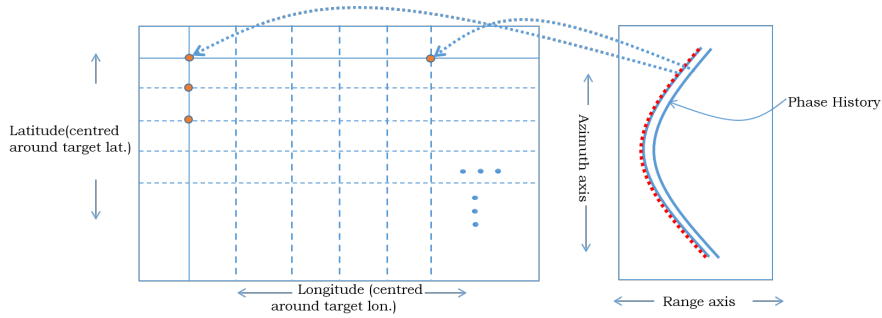
Figure 3.5: A pictorial representation of the process of extraction of phase history from the range interpolated data and the data being matched to every cell on the grid

Azimuth Compression

Each matched phase history is extracted, multiplied and summed with a compensated phase. The process is repeated until all similar bistatic phase histories are extracted. The compressed data is then transferred back to the grid and can be expressed as,

$$s_{final} = \sum s_{intp} \cdot exp \left\{ -j2\pi f_0 \left(\frac{(r_{phase}\,(\eta) - r(\eta_0))}{c} \right) \right\} \tag{3.8}$$

where, s_{final} is the final image obtained after compression and phase compensation, r_{phase} is the phase histories for every azimuth time η, $r(\eta_0)$ is the minimum range from the centre of total aperture length (mid point of total aperture) , in bistatic case , it is the mean of two slant ranges obtained from transmitter and receiver.

3.2.1 Introduction to WGS–84 coordinate System

The World Geodetic System 1984 standard (WGS-84), is a standard coordinate system used as a reference for the Earth. The system when expressed in Cartesian coordinates (X, Y, Z) has its origin as the center of the Earth, the Z axis runs from origin to the North pole, the Y axis from origin to the reference meridian and X axis is chosen such that a clockwise coordinate system is created. According to the WGS-84, the Earth is assumed to be in the shape of an oblate spheroid,i.e., at any given latitude, the cross section is circular and an elliptical cross section through any meridian. The fundamental coordinates , (X, Y, Z) is expressed in meters and can be converted to latitude, longitude and altitude (lat-lon-alt). In practice, the final image obtained after processing the SAR data is often expressed in terms of the ECEF coordinate system if the BP algorithm is applied. The global positioning is well understood by latitude, longitude and altitude coordinates, but, since the Cartesian coordinate system is easier to compute ,the point target is given in lat-lon-alt and calculated in Cartesian coordinate system. The Fig. 3.6 shows an example of the WGS-84 system.

WGS-84 coordinate system
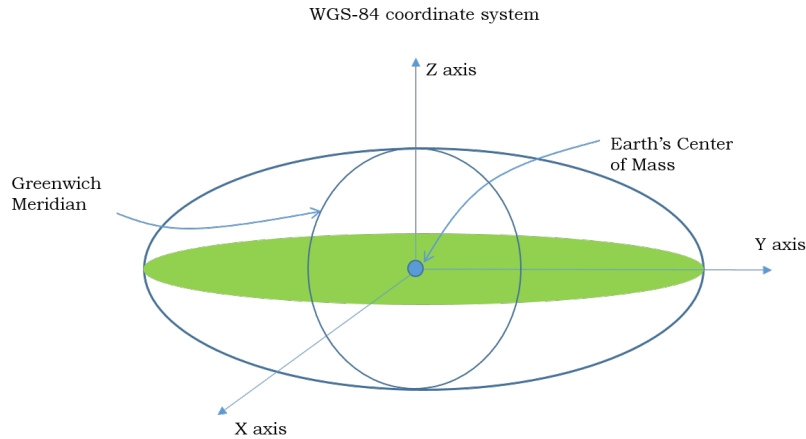
Figure 3.6: Representation of WGS-84 coordinate system. Each dimension of the axes is computed with respect to the Earth's center of Mass.

The length of the Earth's axes is given by the following equations [14]:

$$Semi-major\ axis: a = 6,378,137\ m,$$
$$Semi-minor\ axis: b = 6,356,752.3142\ m. \tag{3.9}$$

3.2.2 Simulation Results and Performance Analysis

Simulations

The raw data and the range compressed data are similar to the results obtained in Chapter 2. Hence the following results deal with final image obtained after the implementation of the back projection algorithm for different bistatic geometries. The following parameters are used for the simulation. Considering the STEREOID configuration, the performance is evaluated for a maximum baseline of 250 km.

Parameter	Values
Bandwidth	42.5 MHz
Chirp duration	53.4μ sec
PRF	1870 Hz
Orbit	Sun Synchronous
Target (lat, lon)	$(0.001°, 0°)$
Look Angle	$35°$
Grid Length, Latitude	111 m
Grid Length, Longitude	111 m
Grid Interval,Latitude	0.1m
Grid Interval, Longitude	0.1m

Table 3.1: Parameters for Bistatic Back Projection

(a) Baseline = 0 km

(b) Baseline = 50 km

(c) Baseline = 100 km

(d) Baseline = 150 km

(e) Baseline = 200 km
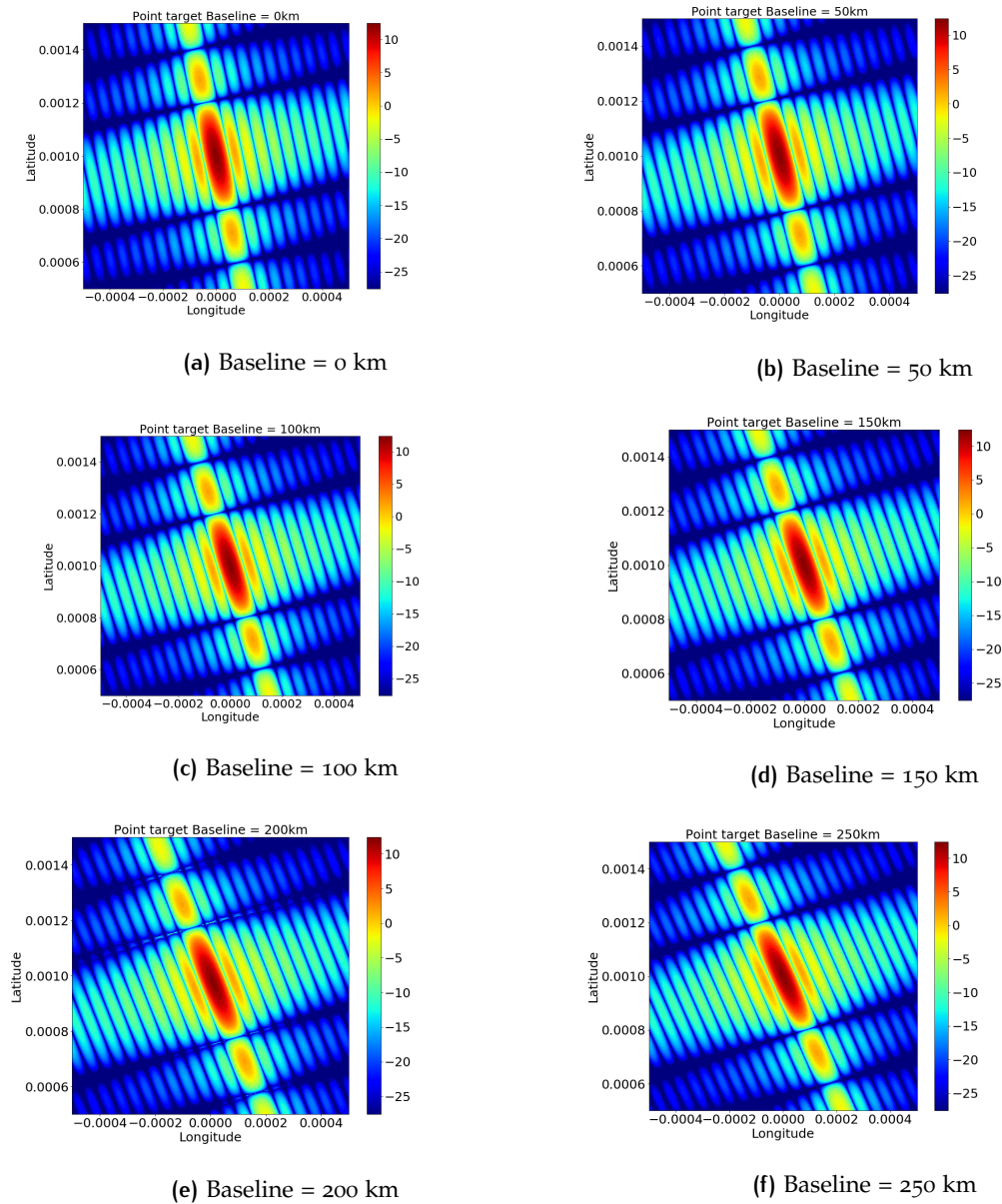
(f) Baseline = 250 km

Figure 3.7: The point target simulations is expressed in dB for different baseline configurations varying from 0 km to 250 km. The focused image was computed based on the position and velocity vectors of the satellite. For a baseline of 0km, it can be observed that the target is in the monostatic scenario. The target appears to be tilted due to the introduction of orbit and angle between the flight direction and the latitude. During the experimental phase, there may be a case when the along-track baseline is 0 km, the target in monostatic case would appear similar to the results obtained in Chapter 2. As the baseline increases to maximum of 250 km , the tilt of the target also increases.

Performance Analysis

Iso-Doppler and Iso-Range lines are used for evaluation for sidelobes and the gradient of Iso lines for evaluation of resolution as shown in Fig 3.8. The following figure has an along track baseline of 250km. The blue dotted lines indicate the iso-range and iso-doppler lines. The red dotted line is the area occupied by the resolution cell.
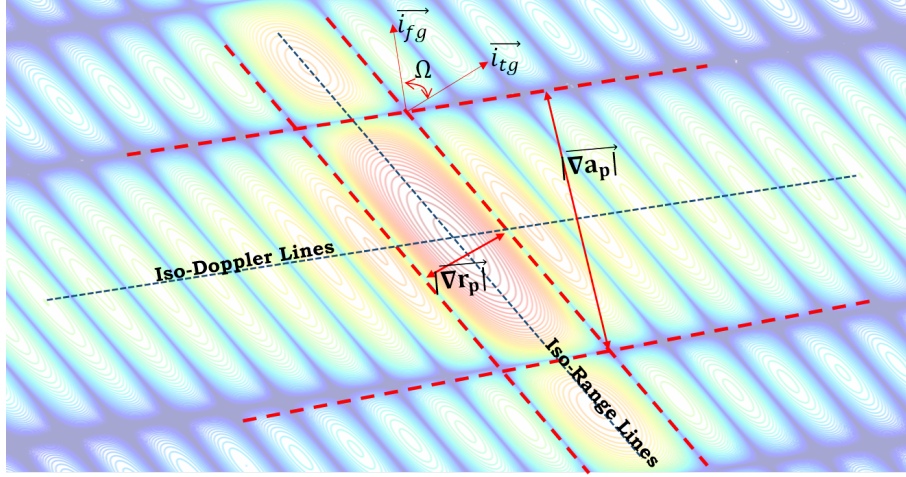
Figure 3.8: A representation of the Iso-Range and Iso-Doppler lines (blue dotted lines) for evaluation of sidelobes. The corresponding gradient direction of the iso lines $\vec{i}_{tg}$ and $\vec{i}_{fg}$ (red arrows), indicate the direction of best possible resolution that can be achieved. The angle Ω is the angle made by the gradient lines. The red dotted lines indicate the area occupied by the resolution cell.

It can be noted from the figure that the gradient to the iso-range and iso-Doppler lines , $\vec{i}_{tg}$ and $\vec{i}_{fg}$ respectively, make an angle Ω, which can be expressed as,

$$\Omega = cos^{-1}\left(\vec{i}_{tg} \cdot \vec{i}_{fg}\right). \qquad (3.10)$$

The Iso-Range and Iso-Doppler lines are depicted in Fig. 3.9. From the figures of iso-lines it is observed that the lines move in the direction highest magnitude to the lowest one. When these lines are expressed as contour lines, they can be used to evaluate the performance of the target. This is depicted in Fig. 3.10. The 3 dB resolution of range and azimuth obtained from the Iso-range and Iso-Doppler line is evaluated, refer to Fig. 3.11 and Fig. 3.12, which is evaluated for a bistatic scenario for a baseline of 250km. The lines are not perpendicular to each other due to the bistatic configuration and long along track baseline configuration (250km). Due to the the bistatic orientation, the practical bistatic resolution can be expressed as,

$$\bigtriangledown r_p = res_r sin(\Omega), \qquad (3.11)$$

$$\bigtriangledown a_p = res_{az} sin(\Omega), \qquad (3.12)$$

where, res_r and res_{az} are the resolution in azimuth and range obtained from iso-lines and $\bigtriangledown r_p$ and $\bigtriangledown a_p$ are the practical bistatic resolutions.
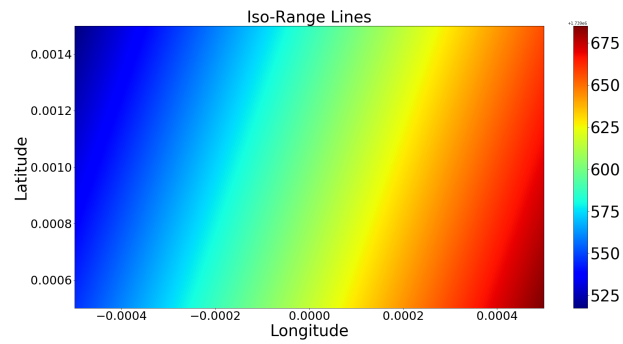
(a) Variation of Iso-Range Lines
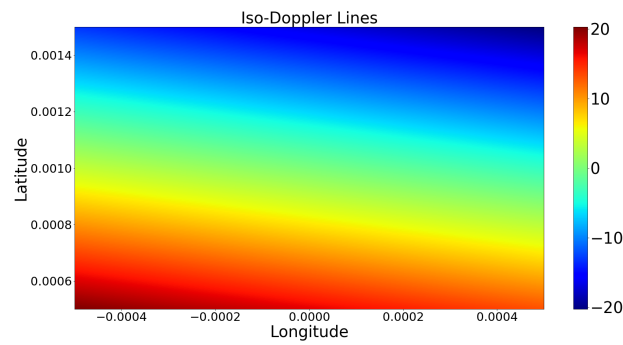
(b) Variation of Iso-Doppler Lines

Figure 3.9: The Iso Range and Iso Doppler Lines are depicted. The variation of the lines is depicted for a baseline separation of 250km. The lines can vary for different SAR geometries.
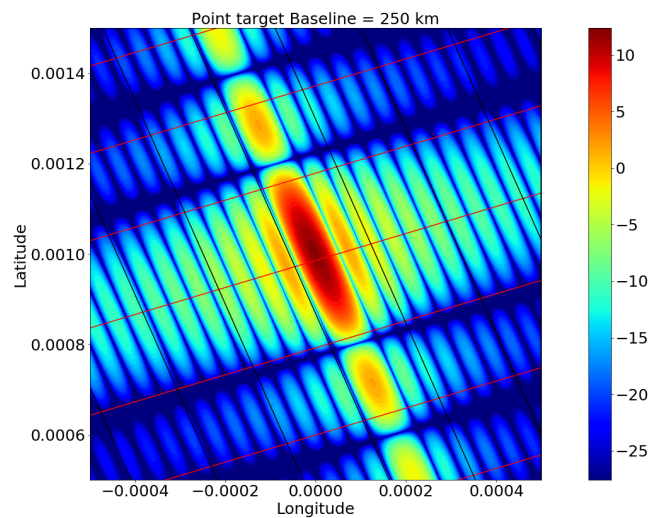
Figure 3.10: The figure depicts a point target for a baseline separation of 250 km. The Iso-Range lines (black) and Iso-Doppler lines (red) are contour lines superimposed on the plot. The Iso lines when finely interpolated pass through the sidelobes which help in evaluation of parameters such as ISLR and PSLR.
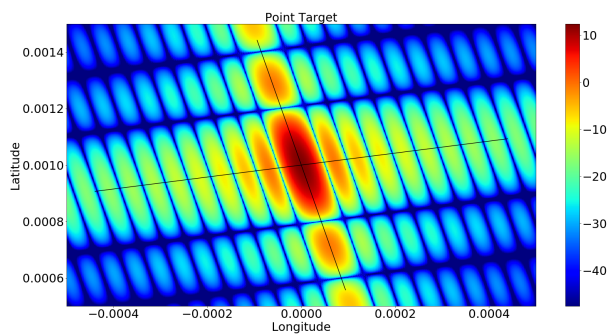
(a) Range Cut
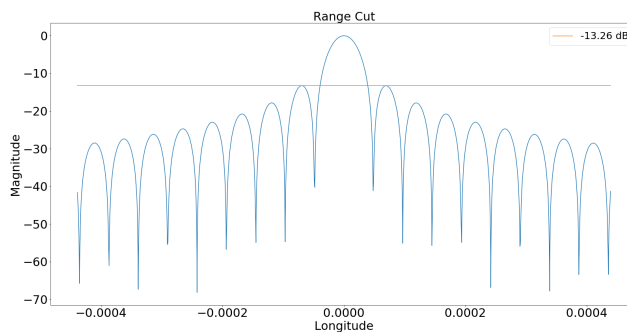
(b) Range Cut
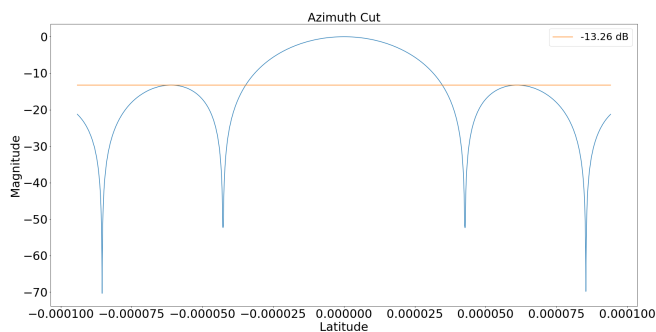
(c) Doppler Cut

Figure 3.11: The Iso Range and Iso-Doppler Lines are used to cut the data through range and azimuth of the monostatic for a separation of 0 km. The -13.26 dB line indicates the level of sidelobes with respect to main lobe.

(a) Range Cut

(b) Range Cut

(c) Doppler Cut
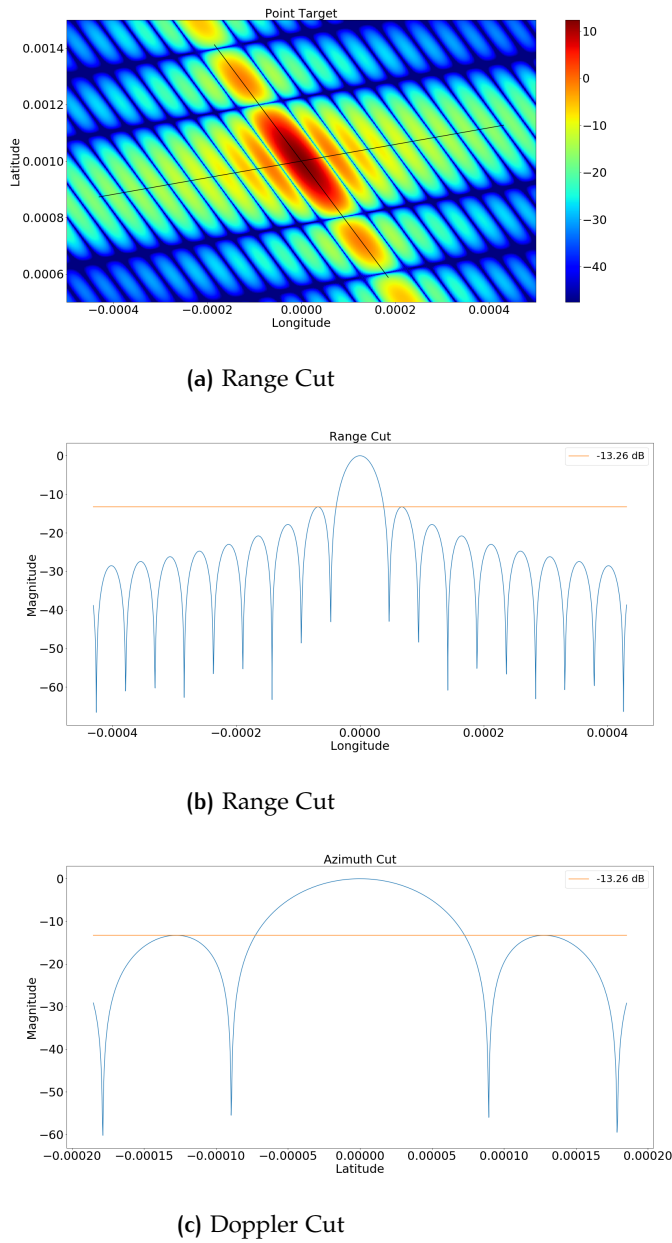
Figure 3.12: The Iso Range and Iso-Doppler Lines are used to cut the data through range and azimuth of the bistatic data for a separation of 250 km. The -13.26 dB line indicates the level of sidelobes with respect to main lobe.

3.3 COMPARISON OF MONOSTATIC AND BISTATIC SCENARIO

The following tables provide a comparison between the performance analysis of BP for monostatic and bistatic scenario for a baseline separation of 250km.

Parameter	Direction	Theoretical	Practical
Resolution(m)	Range	4.8	4.8
Resolution(m)	Azimuth	21.79	20.04
PSLR (dB)	Range	-13.26	-13.26
PSLR (dB)	Azimuth	-13.26	-13.26
ISLR (dB)	Range	-9.7	-9.54
ISLR (dB)	Azimuth	-9.7	-9.03

Table 3.2: Performance analysis for Monostatic Scenario

Parameter	Direction	Theoretical	Practical
Resolution(m)	Range	4.8	4.8
Resolution(m)	Azimuth	22.96	21.31
PSLR (dB)	Range	-13.26	-13.26
PSLR (dB)	Azimuth	-13.26	-13.26
ISLR (dB)	Range	-9.7	-9.54
ISLR (dB)	Azimuth	-9.7	-9.03

Table 3.3: Performance analysis for Bistatic Scenario

From Table 3.2 and Table 3.3, it can be observed that in the monostatic case the azimuth resolution is comparatively lesser than that in the bistatic case. Since the baseline separation increases in bistatic scenario, the resolution along azimuth worsens. The practical value of bistatic resolution along azimuth is comparatively lesser than the theoretical value due to introduction of orbit and the orbit is not rectilinear. The sidelobes evaluated by the parameters ISLR and PSLR are almost close to the theoretical value which indicates the influence of side lobes on the main lobe is comparatively lesser.

3.4 CONCLUSION

In this Chapter, the time domain backprojection algorithm was chosen due to its robustness and accuracy. The algorithm was implemented for different bistatic geometries. The simulated point target was moved to orbit geometry and evaluated in latitude and longitude coordinates as in most practical applications lat-lon coordinate system is used. The bistatic data is evaluated using the gradient of Iso-lines as a coupling effect of range and azimuth occurs due to the large along track baseline between the transmitter and the receiver. It was observed that the resolution evaluation for a bistatic case is not direct and simple as that observed in the monostatic scenario.

4 | BISTATIC TOPS IMAGING ON STEREOID

4.1 INTRODUCTION TO TERRAIN OBSERVATION BY PROGRESSIVE SCANS (TOPS)

Terrain Observation by Progressive Scans (TOPS) is a multiswath scanning burst mode that provides enhanced swath width in comparison to the Stripmap mode [17]. A general intuitive principle of SAR is that, given fixed antenna dimensions, the illumination time for each target is inversely proportional to the width of the illuminated scene. This means that, in order to obtain a scene N-times larger, the resolution in azimuth shall also degrade at least of a factor N. In order to extend the range of incidence angles without using an antenna N times larger in azimuth and N times narrower in elevation, the commonly adopted approach is to divide the total scene extent into N subswaths and to steer electronically the beam in elevation to sense each one of them in turn. Each subswath is then illuminated for an interval of time denoted as the burst time, after which the antenna scans the following subswath. Two different techniques are currently implemented on satellites to realize this multiswath concept. The first mode, recalled as Scan mode or ScanSAR, is characterized by short burst compared to the total aperture time. Several bursts are hence used to sythesize an image. The second mode, recalled as TOPS, sets the equivalence between the burst and aperture integration time. It follows that each target is illuminated by a single burst and that the antenna is steered in azimuth to cover N time more ground than a stripmap system in the same temporal interval (hence with a positive doppler centroid rate).TOPS mode eliminates the effects of azimuth varying ambiguities and scalloping effects. Terra SAR-X implemented and demonstrated TOPS for the first time [17].

4.1.1 Comparison of TOPS to Scan mode

In Scan SAR, to obtain coverage for a broader swath width, the antenna beam is scanned over several subswaths. Since the illumination time is shorter compared to Stripmap, the phase history of each target is reduced to fragments, or bursts, of the total history, leading to reduced target bandwidth and degraded azimuth resolution. The Fig. 4.2 shows that two targets placed at different azimuth positions are illuminated by different portions of the antenna pattern i.e., portions with different amplitudes and different Doppler frequency. Although the targets have similar total bandwith, this amplitude diversity leads to some special artifacts. It causes a periodic amplitude modulation, also known as scalloping effect. This effect would make the calibration of Scan SAR more difficult and would require additional information on noise floor and Doppler centroid to overcome the difficulty. Another artifact would be an azimuth varying resolution and ambiguity ratio. The effect of these artifacts can mostly be seen at the targets placed closed to the edge of the antenna pattern than those placed in the middle.
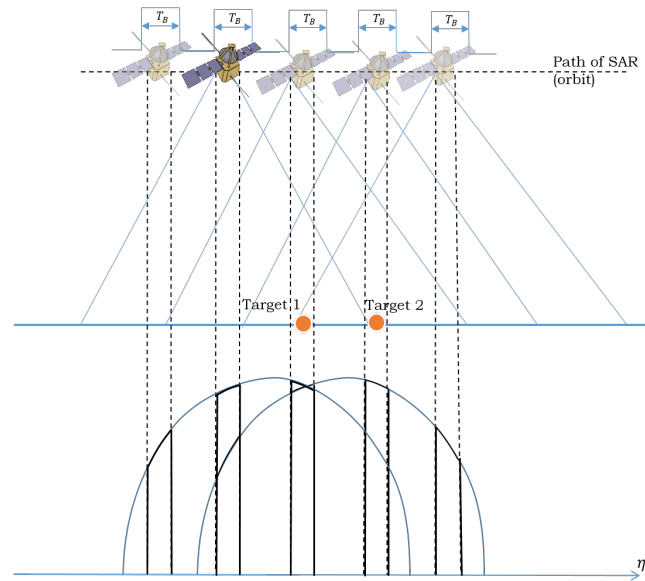
Figure 4.1: Scan SAR acquisition geometry of two point target on the ground with T_B as the burst time. It can be noted that only a small portion of the targets are illuminated which may give rise to special artifacts.
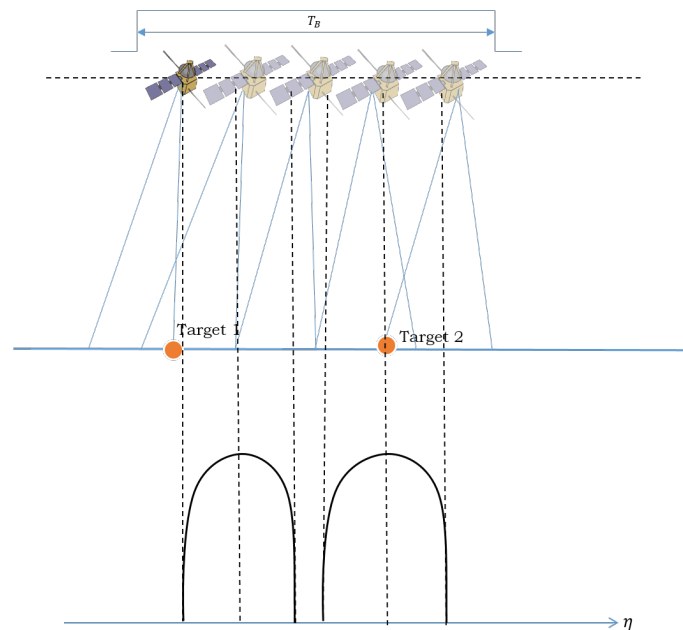
Figure 4.2: TOPS SAR acquisition geometry of two point targets on the ground with T_B as the burst time. Each target is illuminated separately for a long burst duration, which helps avoid scalloping effects even when the targets are placed at the end of the swath.

To overcome this effect, TOPS mode is taken into consideration.The TOPS mode utilizes long bursts of pulses to scan one or more targets on the ground. The antenna is rotated backwards and forwards during the scan. The received signal obtained from the sensor is from a much longer strip than that obtained from a conventional Stripmap mode. This helps the antenna switch to different subswaths. A consequence of the TOPS operating mode is that targets located at different azimuth positions are imaged with different squint angles; Similarly to ScanSAR, the azimuth signals have a shorter bandwidth, at least n times lower than the one that could be achieved in the Stripmap

case where n is the number of illuminated swaths.
The bandwidth of each target for a dwell time of T_D is given by the following equation,

$$B_a = |k_R| \cdot T_D, \tag{4.1}$$

where, k_R the Doppler rate is given by,

$$k_R = -\frac{2v_s^2}{\lambda R_0}, \tag{4.2}$$

where, R_0 is the slant range and v_s is the average velocity of the sensors in the bistatic case.

The signal characteristics of TOPS can be explained through a time-frequency diagram. The following Fig. 4.3 represents a time frequency diagram of TOPS mode consisting of four targets, P1, P2, P3 and P4. The phase histories of each of these targets are represented by a thin black line. The phase history has a negative slope and a Doppler rate of k_R. The shaded blue region is the azimuth antenna pattern (AAP) weighting. As the antenna sweeps with time, a Doppler centroid rate is obtained represented by the upright slant line. The Doppler centroid rate, k_a is given by,

$$k_a = -\frac{2v_s}{\lambda}k_\psi, \tag{4.3}$$

where, k_ψ is the steering rate.
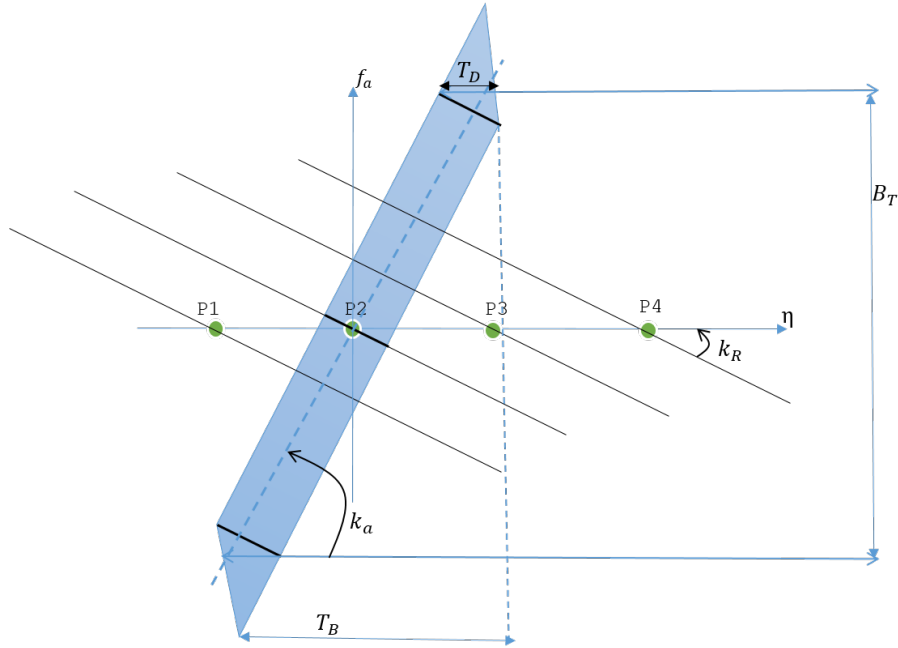
Figure 4.3: Time frequency diagram of TOPS for four targets, P1, P2, P3, and P4. The diagram is plotted for frequency f_a against the azimuth time η. It can be observed that the every target receives a dedicated amount of illumination, for a dwell time of T_D for a Doppler centroid rate, k_a. The Doppler rate is given by k_R, burst time as T_B and Doppler Bandwidth, B_T.

It can be observed from the above Fig. 4.3 that the targets placed at different azimuth obtain the same illumination and the burst is longer which prevents the artifacts observed in Scan SAR. The azimuth resolution for TOPS scenario, $\vec{\nabla}a_{TOPS}$, is given by,

$$\vec{\nabla}a_{TOPS} = \frac{1}{T_D|\vec{\nabla}f_g|}\vec{i}_{fg}, \tag{4.4}$$

where, $\vec{i}_{fg}$ is the unit vector perpendicular to the iso-Doppler lines, T_D is the dwell time given by,

$$T_D = \frac{B_f}{k_r + k_a},\tag{4.5}$$

where B_f is the total badwidth for the whole aperture given by,

$$B_f = -\frac{2v_s}{La},\tag{4.6}$$

where, v_s is the sensor velocity and La is the total synthetic aperture length. $\vec{\nabla f_g}$ is the ground projection of the Doppler gradient. The above equation holds for bistaic configuration of STEREOID when the Doppler gradient is computed for a bistatic geometry.

4.2 STEREOID RECEIVER ANTENNA CONFIGURATION

4.2.1 Antenna Alignment

In a bistatic SAR system, the attitude and the antenna pointing is of great importance when considering variable baseline configurations [24]. The optimum attitude law is mission specific and can dependent on many factors [25]. The STEREOID receiver antenna, Rx, follows a dual antenna configuration , each antenna separated at a maximum distance of 5m on the same receiver platform. The boresight of the receiver antenna is mechanically oriented such that points to the center of the swath illuminated by the Sentinel transmitter. This does not align the antenna footprints on the ground. This leads to misalignment of the principal axes (u and v axes) of transmitter with the receiver and when the transmitter is steered in azimuth or elevation then a 2D steering is required for the receiver antenna.

When large along track baselines are considered between the transmitter and receiver, then the observation from the receiver is heavily squinted. Therefore, the axes u and v are not orthogonal on the ground. To overcome this problem, antenna steering is introduced. The bistatic attitude law can be defined in two ways: by elevation plane alignment and by azimuth plane alignment.

For the STEREOID bistatic TOPS mode, the elevation plane alignment is chosen. The goal of this method is to align the cross-section of the receiver elevation steering plane with the ground , with respect to the transmitter elevation steering plane, i.e., the zero Doppler plane with the ground. Hence the long side of the receiver antenna array is normal to the elevation steering plane as shown in Fig. 4.4.
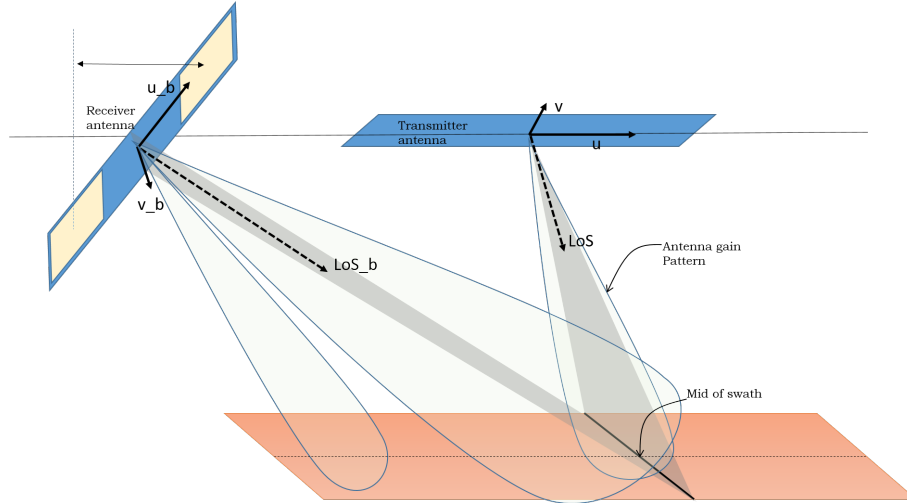
Figure 4.4: The alignment of dual antenna configuration of receiver and transmitter is depicted in the figure. The antenna is placed such that it points to center of the footprint illuminated by the Sentinel transmitter with LoS and LoS_b as the line of sight, v and v_b are the elevation axes and u and u_b are the azimuth axes of the passive radars of the transmitter and receiver respectively.

The line of sight of the receiver antenna, LoS_b can be given by the following equation,

$$L\vec{o}S_b = \frac{\vec{P_{ref}} - \vec{P_{Rx}}}{||\vec{P_{ref}} - \vec{P_{Rx}}||},$$

(4.7)

where, $\vec{P_{ref}}$ is the reference point on the swath, P_{Rx} is the position vector of the receiver. The orientation of the long antenna axis of STEREOID, $\vec{U_b}$ can be derived through a few steps. The projection of Sentinel-1 incidence plane with the ground is computed as,

$$\vec{E} = \vec{u} \times \vec{n_{ref}}$$

(4.8)

where, $\vec{u}$ is the long axis of Sentinel-1 and $\vec{n_{ref}}$ is the local normal to the ground. Then the long axis of STEREOID $\vec{u_b}$ is given by,

$$\vec{u_b} = \frac{\vec{E} \times L\vec{o}S_b}{||\vec{E} \times L\vec{o}S_b||}$$

(4.9)

4.3 DUAL ANTENNA BEAMFORMING

SAR system usually operates in different modes as discussed in Chapter 1. In general, beamforming means "pointing" a radiation of antenna array and shaping the beam. Beamforming in an array achieved by applying a convenient amplitude weight and phase shift to the elements of the array. This can be done in two ways- analog beamforming and digital beamforming. Analog beamforming suffers from various disadvantages such as high weight, low efficiency, high power consumption, difficult caliberation and so on [26]. Hence digital beamforming techniques are preferred. Digital beamforming on receive is implemented on STEREOID. In this method, the array antennas transmit signals and on reception, the signals from each of the arrays are first amplified, down converted and digitised for processing. Standard equations of raw data generation from a dual antenna is derived based on the following Fig. 4.5 depicting a linear phased array antenna.
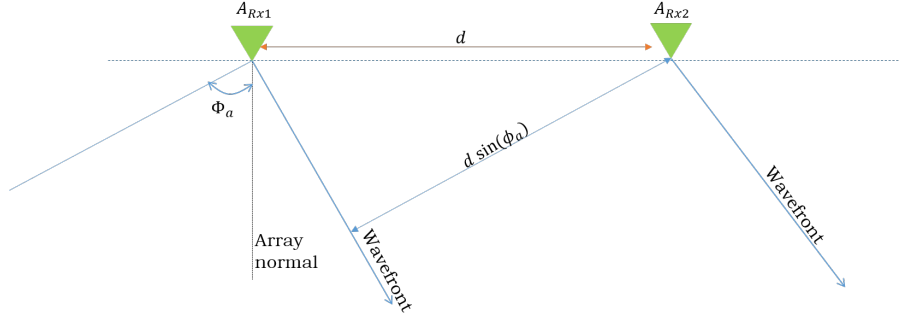
Figure 4.5: A_{Rx1} is the first phased array antenna in the receiver. A_{Rx2} is the second phased array receive antenna separated at a distance d. A_{Rx1} makes an angle ϕ_a the angle associated with the direction of arrival of the wave.The phase shift between the two antennas which is given by $d\ sin(\phi_a)$.

Assuming y_1 as the output signal from first phased array antenna in the receiver and y_2 is the output signal from the second phased array antenna . y_{tot} is the total data from the receiver, the following equation is derived as:

$$y_{tot} = y_1 + exp(j\alpha)y_2, \qquad (4.10)$$

where, α is the phase shift introduced which helps the radiation from the antenna array point to a required direction. Note that y_2 can further be expressed as,

$$y_2 = y_1\ e^{\left(j\frac{2\pi}{\lambda}dsin(\phi_a)\right)}, \qquad (4.11)$$

where, ϕ_a is angle associated to the direction of arrival of the wave. Therefore,

$$y_{tot} = y_1 \left(1 + e^{(j\alpha)}\ e^{\left(j\frac{2\pi}{\lambda}dsin(\phi_a)\right)}\right), \qquad (4.12)$$

$$|y_{tot}| \propto \left|cos\left(\frac{\alpha}{2} + \frac{\pi}{\lambda}dsin\phi\right)\right| \qquad (4.13)$$

Beamforming on STEREOID is done in two ways: beamforming on-board and beamforming on ground.

4.3.1 Beamforming on-board

In this type of beamforming, when the signal is transmitted and received from the antenna, the signal is digitized, processed and sent back to the downlink station. The beamforming on-board has the phase shift α as a function of azimuth time η . Hence $\alpha(\eta)$ is a constant for every pulse but changes with time for every point on the ground. An interesting view of beamforming on-board would be to analyse the convolution of the antenna array pattern with two impulse response functions separated at a distance d depicted as follows,
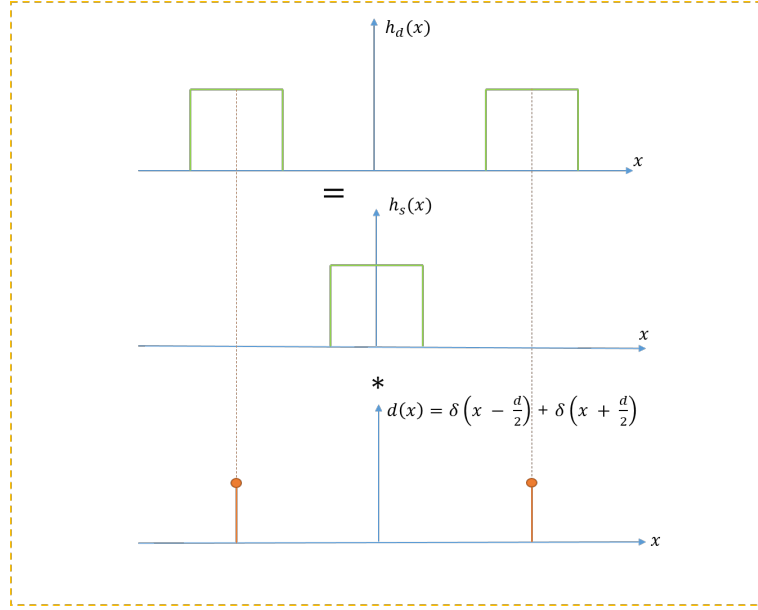
Figure 4.6: A depiction of antenna array patterns as a rectangualr signal convolved with an impulse response separated at a distance d. The fourier transform of the convolved output gives a sinc pattern multiplied with a sine function.

Assume the antenna pattern for the above case is $h(x)$,but for STEREOID, it is dependent on time η and every point on ground $\vec{p}$, therefore $h(\vec{p}, \eta)$ is assumed. The impulse response is given by $\delta(\vec{p}, \eta)$. Therefore,

$$h(\phi_a, \eta) \overset{\mathcal{F}}{\longleftrightarrow} H_f(\phi_a, \eta),\tag{4.14}$$

$$\delta(\vec{p}, \eta) \overset{\mathcal{F}}{\longleftrightarrow} \Delta(\phi_a, \eta),\tag{4.15}$$

Hence the Fourier transform of the above equations can be given by,

$$H_t(\phi_a, t) = H_f(\phi_a, \eta) \cdot \Delta(\phi_a, \eta),\tag{4.16}$$

$$H_f(\phi_a, \eta) \propto sinc\left(\frac{\theta - \theta_0(\eta)}{\frac{\lambda}{l_a}}\right),\tag{4.17}$$

$$\Delta(\phi_a, \eta) \propto cos\left(\frac{\theta - \theta_d(\alpha(\eta))}{\frac{\lambda}{d}}\right),\tag{4.18}$$

where, l_a is the antenna length, d is the distance between the two antennas.

4.3.2 Beamforming on ground

In this method of beamforming, the echo return from the target is collected and is downlinked to the station for further processing. This type of beamforming allows for manual phase addition and also to follow the target precisely. The following equations can help bring the difference between that of on-board and on ground beamforming.
Assuming that y_1 ,y_2 and α is a function of azimuth time η and the values expressed for every point on ground $\vec{p}$,

$$y_1(\vec{p_1}, \eta) = A(\eta)e^{j\phi_{a1}(\eta)},\tag{4.19}$$

$$y_2(\vec{p_1}, \eta) = A(\eta)e^{j\phi_{a2}(\eta)},\tag{4.20}$$

where, $A(\eta)$ is the antenna pattern and ϕ_{a1} and ϕ_{a2} are the phases for every output of the antenna and can be expressed as,

$$\phi_1(\eta) = \frac{2\pi}{\lambda}\vec{R_1}(\eta),\tag{4.21}$$

$$\phi_2(\eta) = \frac{2\pi}{\lambda} \vec{R}_2(\eta), \tag{4.22}$$

Hence the final result can be expressed as,

$$Y_{tot}(\vec{p}_1, \eta) = Y_1(\vec{p}_1, \eta) + e^{j\alpha(\vec{p}, \eta)} Y_2(\vec{p}_1, \eta) \tag{4.23}$$

When the distance d between the antenna is almost 0 then it becomes equivalent to a single array antenna and the gain pattern is wider. As the distance between the two antennas increases, the gain pattern is more narrower and allows for better directivity of the antenna. The following chapter explores the results of such scenarios.

5 STEREOID PERFORMANCE FOR DIFFERENT SCENARIOS

Calibration can be an important aspect in the performance analysis of any system as this can severely affect the imaging quality and estimation of the position of targets. The purpose of this chapter is to study and analyse calibration errors such as amplitude errors and pointing errors for different antenna baseline configurations.

5.1 PERFORMANCE METRIC

5.1.1 Azimuth Ambiguities and its Impact

Azimuth Ambiguities occur due to finite sampling of the Doppler spectrum at pulse repetition frequency (PRF) [28]. Due to repeated PRF intervals, the signal that falls outside the interval folds back into the spectrum. The location of azimuth ambiguities in slant range and azimuth can be given by the following set of equations [27],

$$\Delta_{az,m} \approx m\frac{\lambda \ PRF \ R_0}{2 \ v_s},$$ (5.1)

$$\Delta_{rg,m} \approx \sqrt{{R_0}^2 + {\Delta_{az,m}}^2} - R_0,$$ (5.2)

where, m is the order of the ambiguity, λ is the wavelength, R_0 is the closest slant range or slant range at zero Doppler and v_s is the velocity of satellite. Consider the following figure which depicts the position of ambiguities on the Iso-lines for bistatic STEREOID configuration.
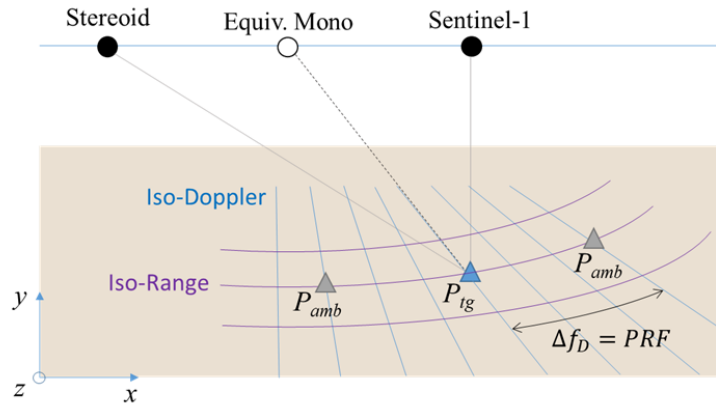
Figure 5.1: Ideal position of ambiguities on the Iso-Doppler and Iso-Range Lines for the bistatic STEREOID configuration. P_{amb} is the position of the ambiguities. P_{tg} is the position of target. The ambiguities are located on the same bistatic slant range of the main target, and are separated in Doppler in an interval equal to the PRF.

The ambiguities are located on the same Iso-Range lines but separated in Doppler by a distance equal to the PRF interval. The azimuth ambiguities spread over multiple range cells due to false compensation of range cell migration. The energy of the ambiguities decreases as the order of the ambiguities increases because of the attenuation provided by the azimuth antenna pattern

[27]. The performance of the ambiguities is evaluated by a parameter known as the Azimuth Ambiguity-to-Signal Ratio (AASR). The AASR measures the influence of azimuth ambiguities on the SAR image.

5.1.2 Computation of AASR

The AASR on the focused image is obtained by computing the energy of the ambiguity to that of the peak energy of the signal. A bounding box is considered around the region of ambiguity and the intensity points that fall within the box are integrated to obtain the energy. The same process is followed for the point target around the region bearing the maximum intensity. Hence AASR can be given by the following expression,

$$AASR = \frac{E\{a_{amb}\}}{E\{p_{trgt}\}} \tag{5.3}$$

where $E\{a_{amb}\}$ is the energy of the ambiguity and $E\{p_{trgt}\}$ is the energy of the point target. The ideal value of AASR is between -15dB to -20 dB.

5.2 STEREOID SIMULATOR CONFIGURATION

The following parameters are the main acquisition parameters for STEREOID configuration commonly used throughout the analysis.

Parameter	Values
Orbit	Sun synchronous
Mode	TOPS
Sentinel-1 Antenna	Phased Array
Sentinel-1 Antenna Dimensions	Length(Azimuth) : 12.3 m Length (Elevation) : 0.84 m
STEREOID Antenna	Dual Phased Array
STEREOID Antenna Baseline Separation	5 m
STEREOID Antenna Dimensions	Length(Azimuth): 1.3 m Length(Elevation) : 0.7869 m
STEREOID Elements	N(Azimuth): 5 N(Elevation) : 10
Number of Subswaths	3
Chirp bandwidth (based on swath)	56.5 MHz, 48.3 MHz and 42.8 MHz
Chirp duration (based on swath)	52.4μs, 62μs and 53.4μs
PRF (based on swath)	1717 Hz, 1451 Hz and 1685 Hz
Burst Length (based on swath)	0.82 s, 1.06 s and 0.83 s

Table 5.1: STEREOID parameters for data acquisition

5.3 PERFORMANCE ANALYSIS

This section deals with the analysis for both methods of beamforming as discussed in Chapter 4. The analysis accounts for the two main relevant factors imparting on the performance : the distance between the two receiver antennas and the pointing errors introduced on the antennas.

5.3.1 Analysis for different antenna baseline configurations

Antenna Patterns for different baseline configurations

The parameters used for the analysis of different baseline configurations are as follows:

Parameter	Values
Subswath	0
Chirp bandwidth	56.5 MHz
Chirp duration	48.3μs
PRF	1717 Hz
Burst Length	0.83 s
Target Location	Lat :0° Lon: 0°
Scene size	Length (along lat):16.7 km length (along lon): 4.4 km

Table 5.2: STEREOID parameters for analysis of different antenna baseline configurations

Transmit Pattern
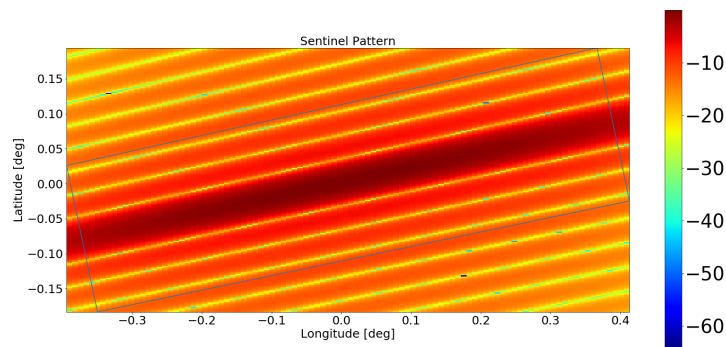
Figure 5.2: Simulation for the transmit pattern of Sentinel-1 with respect to the parameters in Table 5.1. The figure shows pattern at zero Doppler and the rectangular region indicates the beam footprint of the antenna or the region of illumination of the antenna. The region with highest magnitude as indicated by the colorbar and the maximum illumination of target occurs in that region.

STEREOID Receiver Pattern for Different Antenna Baseline
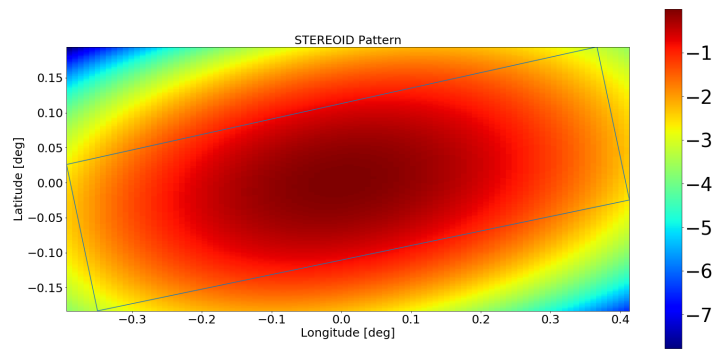
(a) Antenna Baseline: 0 m
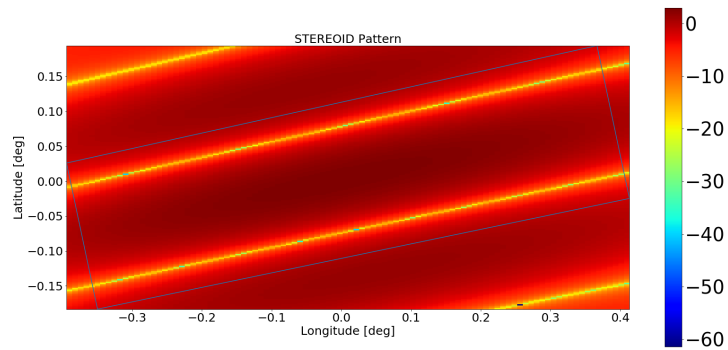
(b) Antenna Baseline: 3 m
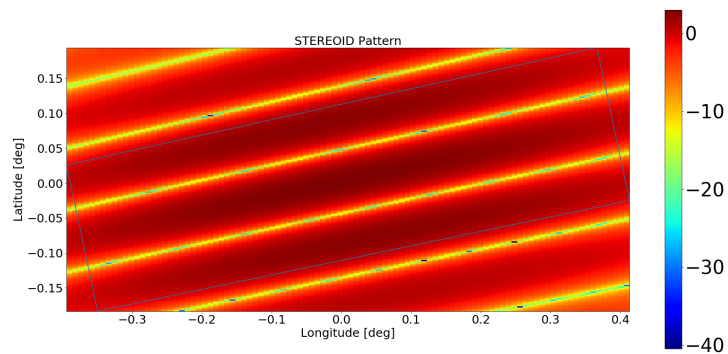
(c) Antenna Baseline: 5 m

Figure 5.3: The simulations of STEREOID antenna pattern as different antenna baseline configurations are shown. When the baseline is almost 0 then the receiver antenna behaves as a single array antenna and the lobes of the pattern are broader. As the baseline increases the lobes of the pattern become narrower, as depicted in Fig.(b) and Fig.(c) which increases the directivity of the antenna.The blue bounding box indicates the beam footprint, i.e., the region of antenna illumination.

Beamforming On-Ground

The following simulations are focused point targets for beamforming on ground with STEREOID antenna baseline configuration ranging between 0 m to 5 m. **Antenna Baseline:** 0 **m**
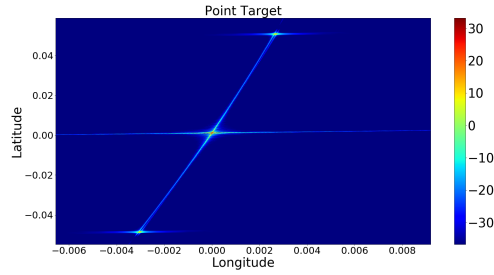
(a) Point Target for antenna baseline of 0 m for beamforming on ground
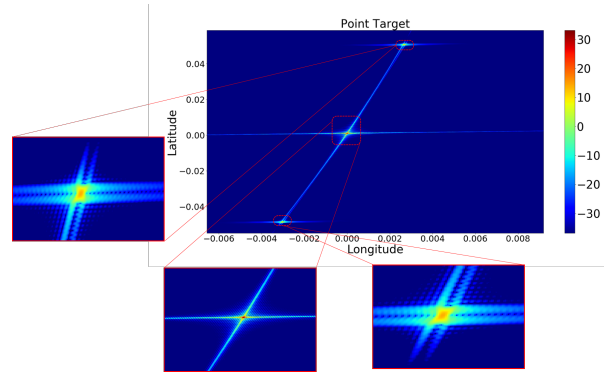
(b) Enhanced images of point target and first order ambiguities
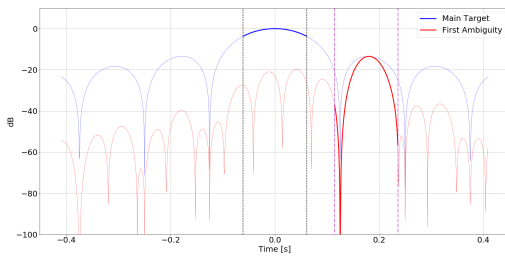
(c) Temporal Pattern
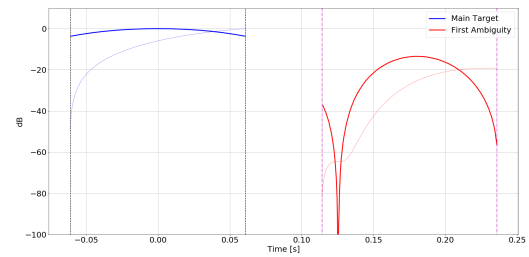
(d) Time Integration Gain pattern

Figure 5.4: Fig.(a) is the simulated point target antenna baseline of 0 m. The figure simulated for a large scene (16.7 km x 4.4 km) shows first order ambiguities on left and right of the target. The enhanced image of the scene is depicted in Fig.(b). Fig.(c) represents the temporal pattern of the main target and the first order ambiguity. The region of maximum intensity of the target (highlighted blue line) and of ambiguity (highlighted red line) is indicated. The difference between the main lobe and the ambiguity is approx. -13.66dB. Fig.(d) for the point target and the integrated values of the ambiguity and the target (indicated by non-highlighted red and blue lines respectively).The region of maximum intensity of the target (highlighted blue line) and of ambiguity (highlighted red line) is indicated.

Antenna Baseline: 3 **m**
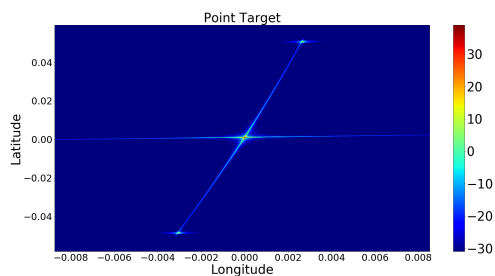
(a) Point Target for antenna baseline of 3 m for beam-
forming on ground
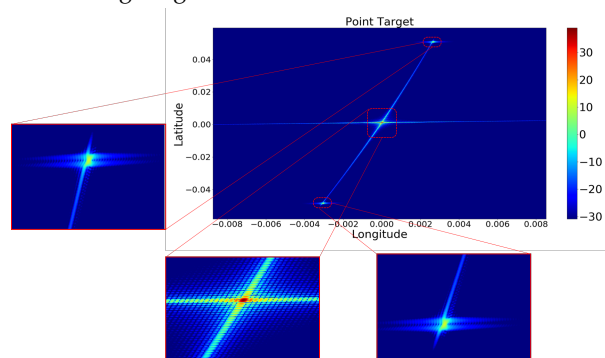
(b) Enhanced images of point target and first order am-
biguities
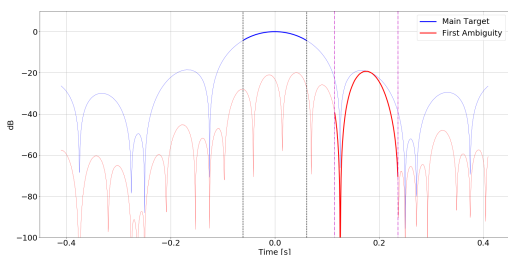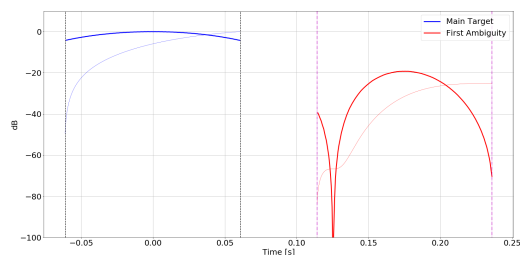
(c) Temporal Pattern

(d) Time Integration Gain pattern

Figure 5.5: Fig.(a) is the simulated point target for the given scene length, target coordinates and for an
antenna baseline of 3 m. The enhanced image of the scene is depicted in Fig.(b). Fig.(c) rep-
resents the temporal pattern of the main target and the first order ambiguity . The region of
maximum intensity of the target (highlighted blue line) and of ambiguity (highlighted red line)
is indicated.The difference between the main lobe and the ambiguity is approx. -20.26dB. Fig.(d)
for the point target and the integrated values of the ambiguity and the target (indicated by non-
highlighted red and blue lines respectively).The region of maximum intensity of the target (high-
lighted blue line) and of ambiguity (highlighted red line) is indicated.

Antenna Baseline: 5 m
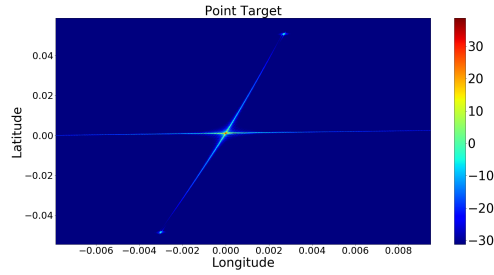
(a) Point Target for antenna baseline of 5 m for beam-forming on ground
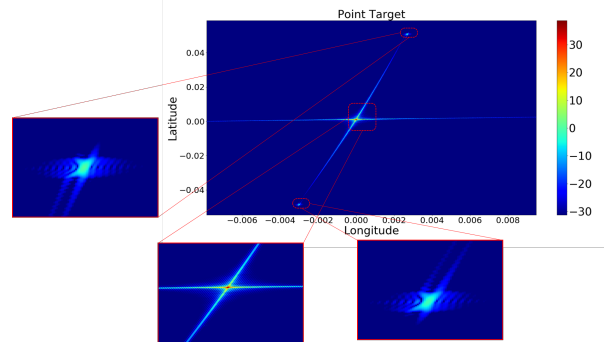
(b) Enhanced images of point target and first order ambiguities.
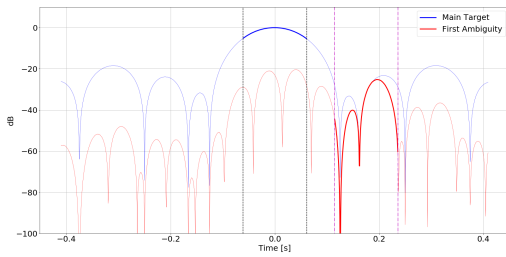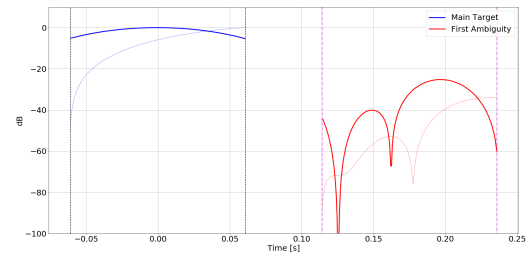
(c) Temporal Pattern

(d) Time Integration Gain pattern

Figure 5.6: Fig.(a) is the simulated point target for the given scene length, target coordinates and for an antenna baseline of 5 m. The enhanced image of the scene is depicted in Fig.(b). Fig.(c) represents the temporal pattern of the main target and the first order ambiguity. The region of maximum intensity of the target (highlighted blue line) and of ambiguity (highlighted red line) is indicated. The difference between the main lobe and the ambiguity goes down to approx. -25.24 dB. Fig.(d) for the point target and the integrated values of the ambiguity and the target (indicated by non-highlighted red and blue lines respectively).The region of maximum intensity of the target (highlighted blue line) and of ambiguity (highlighted red line) is indicated.

Beamforming On-Board: Baseline 0 **m**

The following simulations are for beamforming on-board simulated for a STEREOID antenna baseline ranging from 0m to 5m.
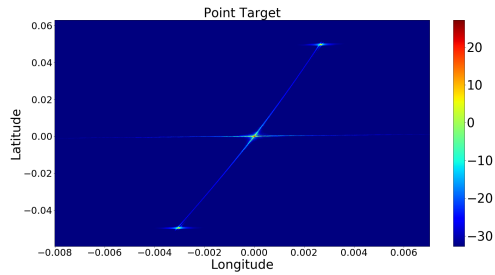
(a) Simulated Point Target for parameters as in Table 5.2
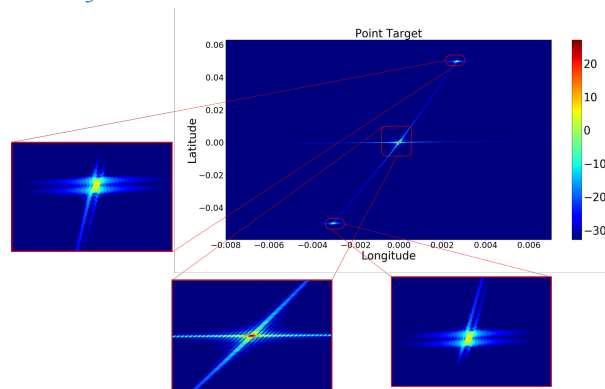
(b) Enhanced depiction of the first order ambiguities and the target
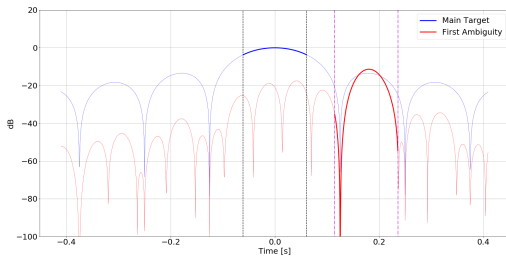
(c) Temporal Pattern
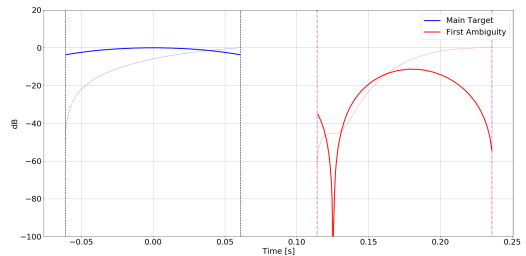
(d) Time Integration Gain pattern

Figure 5.7: Fig.(a) is the simulated point target for beamforming on board. the target was simulated for an antenna baseline of 0 m. The enhanced image of the scene is depicted in Fig.(b). Fig.(c) represents the temporal pattern of the main target and the first order ambiguity . The region of maximum intensity of the target (highlighted blue line) and of ambiguity (highlighted red line) is indicated. The difference between the main lobe and the ambiguity is approx. -11.33 dB. Fig.(d) for the point target and the integrated values of the ambiguity and the target (indicated by non-highlighted red and blue lines respectively).The region of maximum intensity of the target (highlighted blue line) and of ambiguity (highlighted red line) is indicated.

Baseline 3m
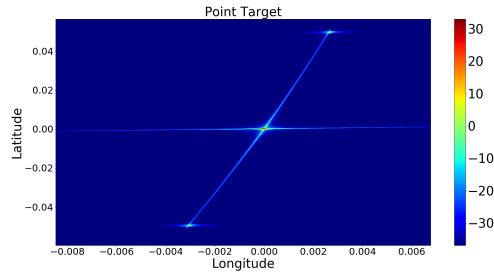
(a) Simulated point target for parameters as in Table 5.2
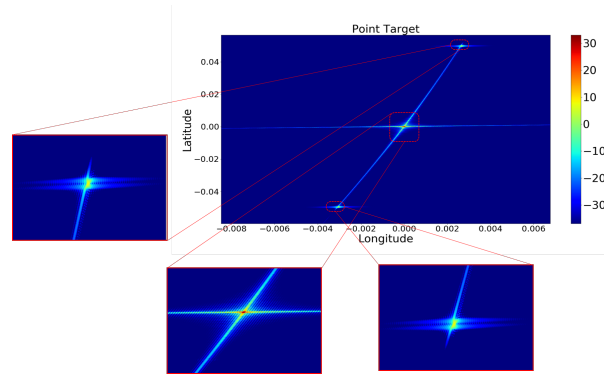
(b) Enhanced depiction of point target and first order ambiguities
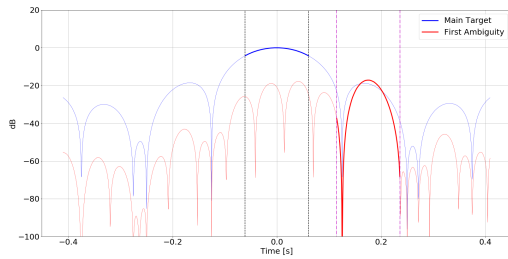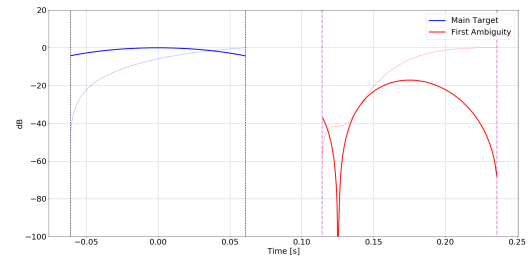
(c) Temporal Pattern

(d) Time Integration Gain Pattern

Figure 5.8: Fig.(a) is the simulated point target for beamforming on board. The target was simulated for an antenna baseline of 3 m.The enhanced image of the scene is depicted in Fig.(b). Fig.(c) represents the temporal pattern of the main target and the first order ambiguity . The region of maximum intensity of the target (highlighted blue line) and of ambiguity (highlighted red line) is indicated.The difference between the main lobe and the ambiguity is approx. -19.21 dB.
Fig.(d) represents the time integration pattern which indicates the integrated pattern for the point target and the integrated values of the ambiguity and the target (indicated by non-highlighted red and blue lines respectively).The region of maximum intensity of the target (highlighted blue line) and of ambiguity (highlighted red line) is indicated.

Baseline 5m

(a) Simulated point target for parameters as in Table 5.2

(b) Enhanced depiction of point target and first order ambiguities

(c) Temporal Pattern

(d) Time Integration Gain Pattern
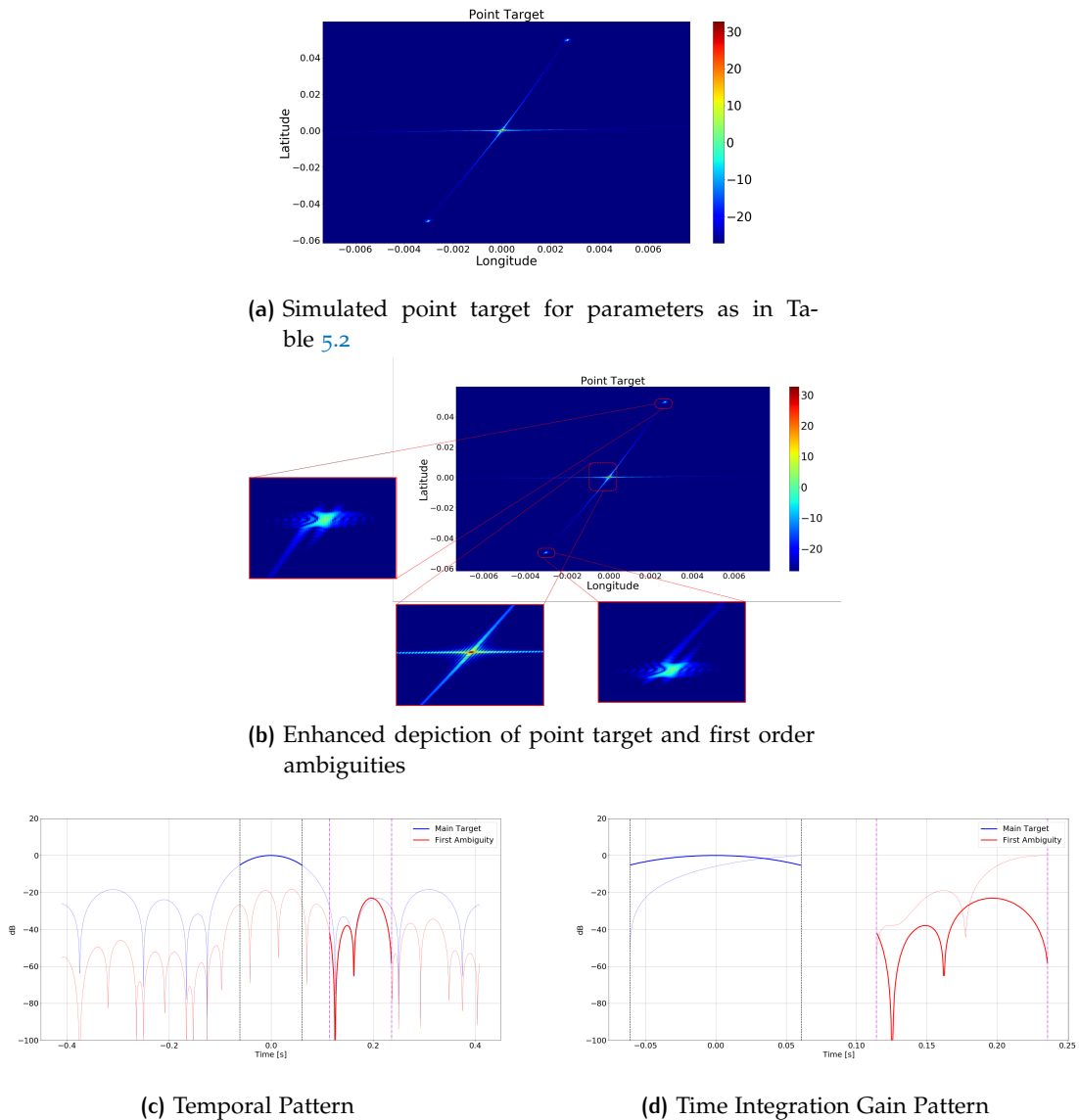
Figure 5.9: Fig.(a) is the simulated point target for the given scene length, target coordinates and for an antenna baseline of 5 m. The figure simulated for a large scene shows first order ambiguities on left and right of the target, situated at the same positions as described for Antenna Baseline of 0 m. The enhanced image of the scene is depicted in Fig.(b). The intensity of the ambiguity reduces as compared to antenna baseline of 0m and 3m. Fig.(c) represents the temporal pattern of the main target and the first order ambiguity . The region of maximum intensity of the target (highlighted blue line) and of ambiguity (highlighted red line) is indicated.The difference between the main lobe and the ambiguity goes down to approx. -23.2 dB.

Fig.(d) represents the time integration pattern for the point target and the integrated values of the ambiguity and the target (indicated by non-highlighted red and blue lines respectively).The region of maximum intensity of the target (highlighted blue line) and of ambiguity (highlighted red line) is indicated.

This section describes the effect of different antenna baseline configurations on the data.The relationship between the baseline of the antenna and the pattern is directly proportional. As the baseline increases, the pattern gets narrower. This can be observed in Fig. 5.3. The above simulations depict the simulated point target for an along track baseline separation of 250 km from STEREOID and Sentinel-1. The target is simulated for different antenna baseline configurations

of STEREOID for beamforming on-board and beamforming on ground. It can be noted that in both methods of beamforming , the common observation is that the intensity of the ambiguities , situated at a (lat, lon) positions of (0.05°, -0.001°) and (-0.05°, 0.001°), reduce as the antenna baseline increases. This can proved with the analysis of the temporal pattern of the target and the first order ambiguity. The temporal pattern brings a comparison of the normalised value of the target and the normalised value of the ambiguity with respect to the target. This can be observed in Fig. 5.4 (c) which shows the difference between main lobe and sidelobe is -13.66 dB. Similarly Fig. 5.5 (c) has an difference of -20.26 dB. From the pattern it can be observed that the magnitude of the ambiguities decreases as the baseline increases due to better directivity of the antenna at bigger baselines. The time integration pattern indicates the integrated values of the target and the ambiguities. They are compared with the pattern alone and the integrated values appear to be a rising curve when compared to the pattern alone.

5.4 ANALYSIS OF TARGETS IN THE BEGINNING AND END OF SWATH

This section discusses on the placing the targets at the beginning and end of every subswath and analysing the AASR for each case. The performance of AASR depends on PRF. Every subswath has a different PRF hence the ambiguities are affected and this can be observed by placing the target at different positions of every subswath. The following parameters are considered for analysis of targets placed at the beginning and end of swath, for beamforming on ground and beamforming on board.

Parameter	Values
Subswath	0, 1, 2
Chirp bandwidth	56.5 MHz, 48.3 MHz and 42.8 MHz
Chirp duration	52.4 μs, 62 μs and 53.4 μs
PRF	1717 Hz, 1451 Hz, 1685 Hz
Burst Length	0.82 s, 1.06 s, 0.83 s
Target Location	Beginning of Swath
	Lat :$-0.05°$
	Lon: $-0.3°$
	End of Swath
	Lat :$0.07°$
	Lon: $0.3°$
Scene size	Length (along lat):16.7 km
	length (along lon): 4.4 km

Table 5.3: STEREOID parameters for analysis of different antenna baseline configurations

Beamforming On Ground

The following section provides simulations for targets placed at the beginning and end of every subswath, for beamforming on ground. **Beginning Sub-Swath** 0
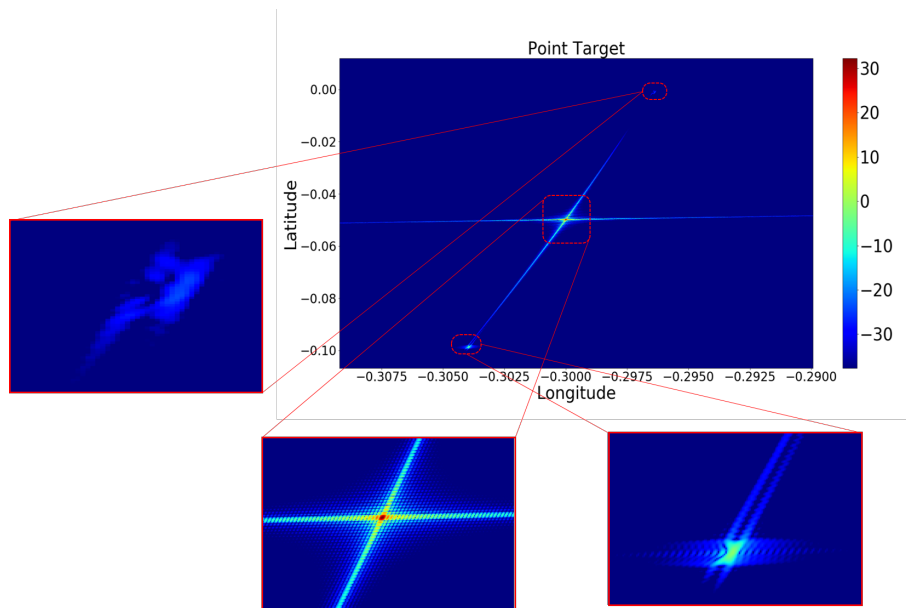
Figure 5.10: Enhanced depiction of the point target and first order ambiguities for beginning of sub-swath 0, AASR = -20.63 dB

End of Sub-Swath 0
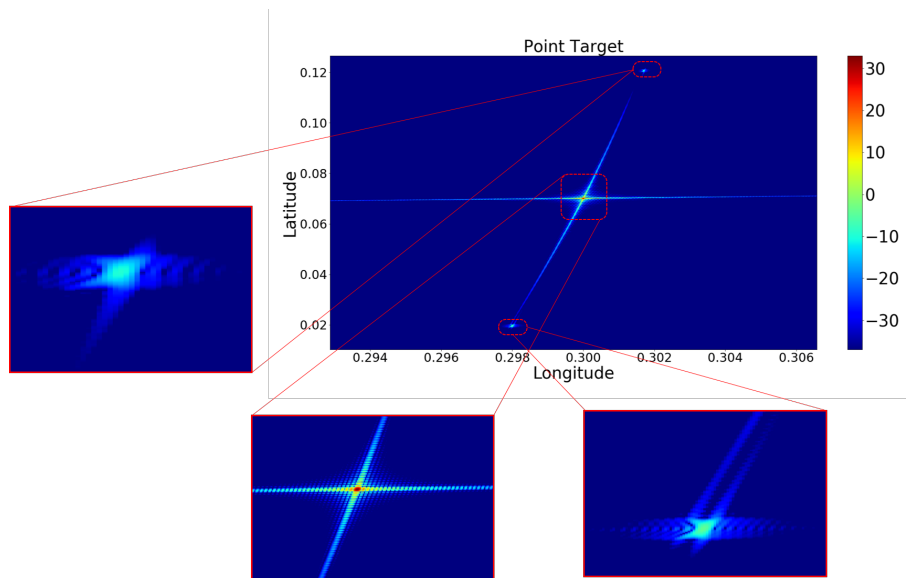
Figure 5.11: Enhanced depiction of the point target and first order ambiguities for end of sub-swath 0, AASR = -20.65 dB

Beginning Sub-Swath 1
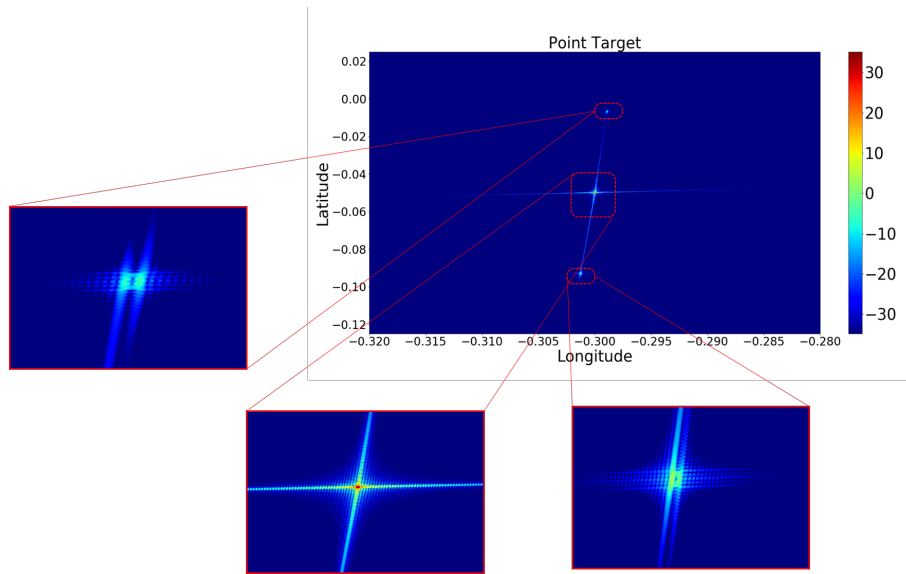
Figure 5.12: Enhanced depiction of the point target and first order ambiguities for beginning of sub-swath 1, AASR = -16 dB

End Sub-Swath 1
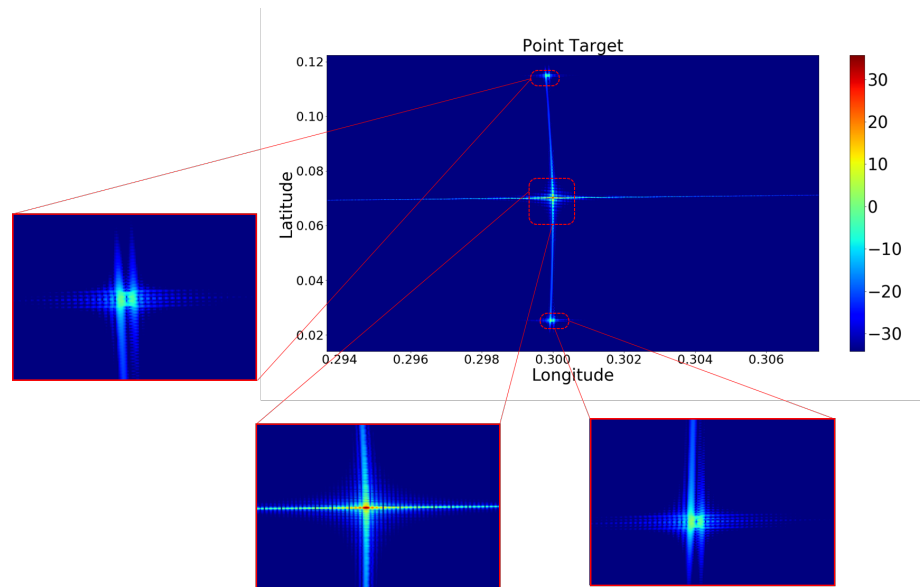
Figure 5.13: Enhanced depiction of the point target and first order ambiguities for end of sub-swath 1, AASR = -16.531 dB

Beginning Sub-Swath 2
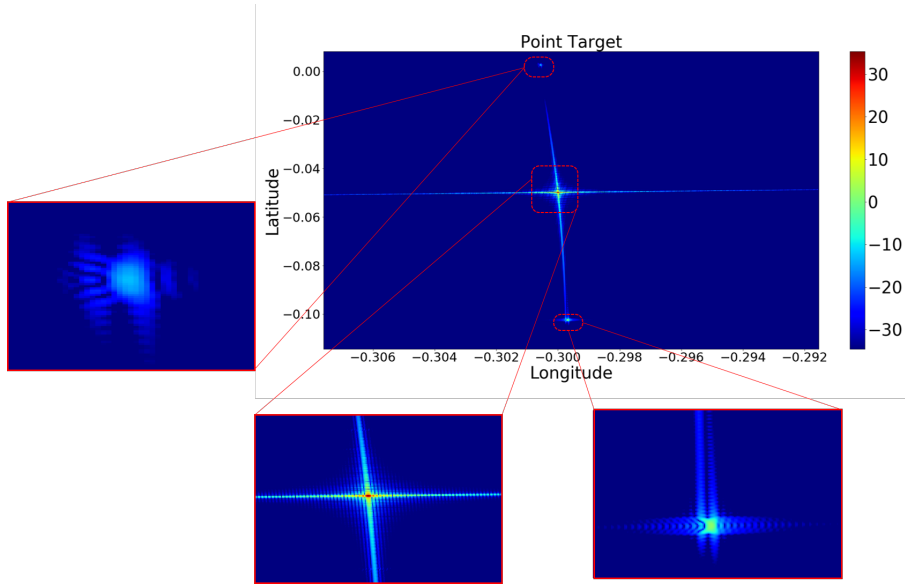
Figure 5.14: Enhanced depiction of the point target and first order ambiguities for beginning of sub-swath 2, , AASR = -20.27 dB

End Sub-Swath 2
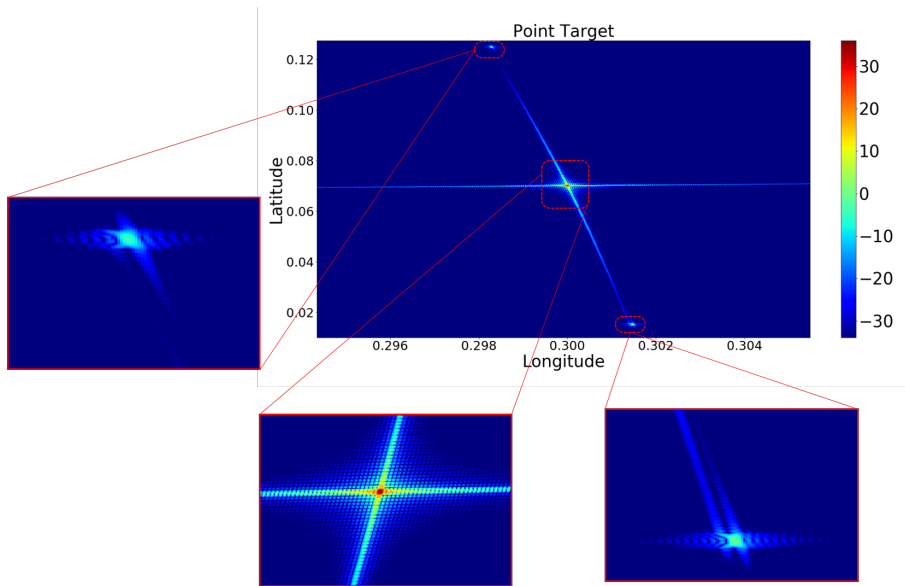
Figure 5.15: Enhanced depiction of the point target and first order ambiguities for end of sub-swath 0, AASR = -20.267 dB

Beamforming On- Board

The following section provides simulations for targets placed at the beginning and end of every subswath, for beamforming on-board. **Beginning Sub-Swath** 0
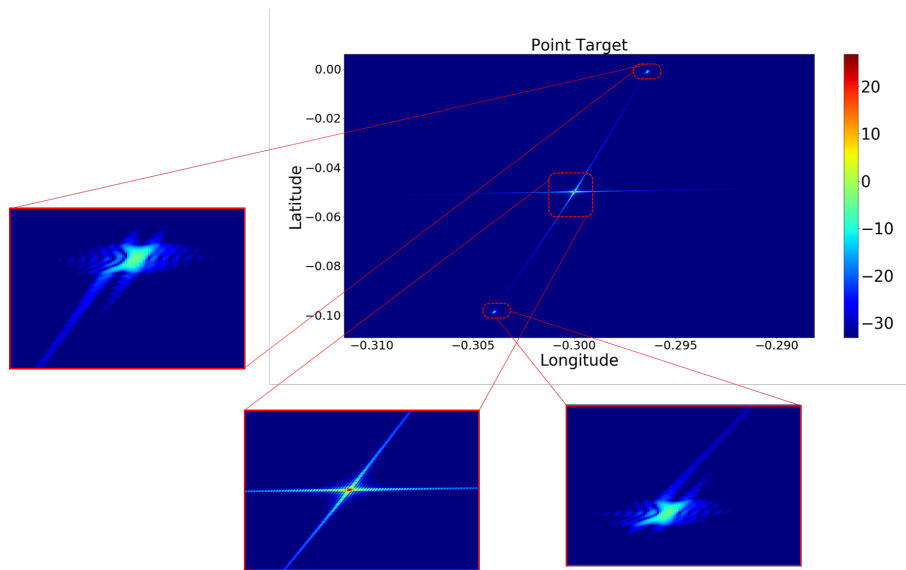
Figure 5.16: Enhanced depiction of the point target and first order ambiguities for beginning of sub-swath 0, AASR = -23.56 dB

End Sub-Swath 0
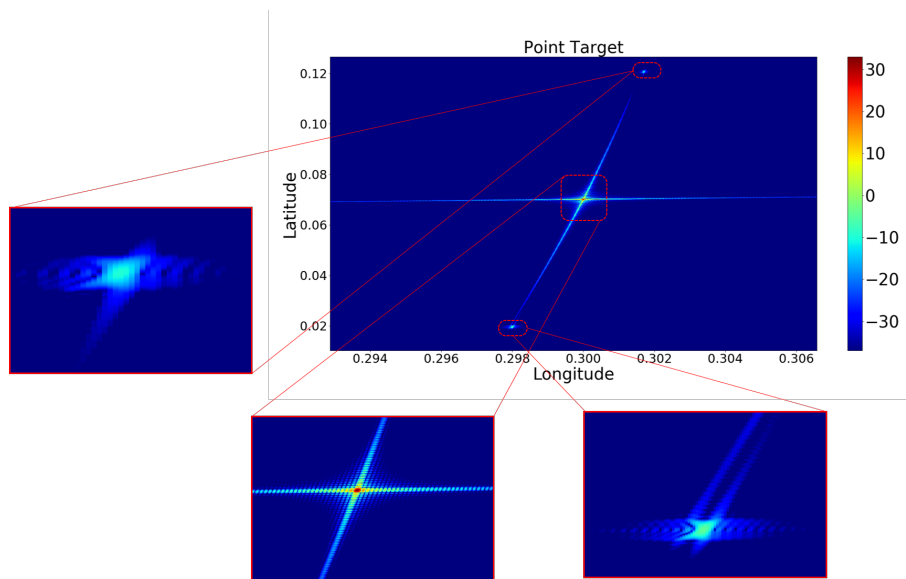
Figure 5.17: Enhanced depiction of the point target and first order ambiguities for end of sub-swath 0, AASR = -24.28 dB

Beginning of Sub-Swath 1
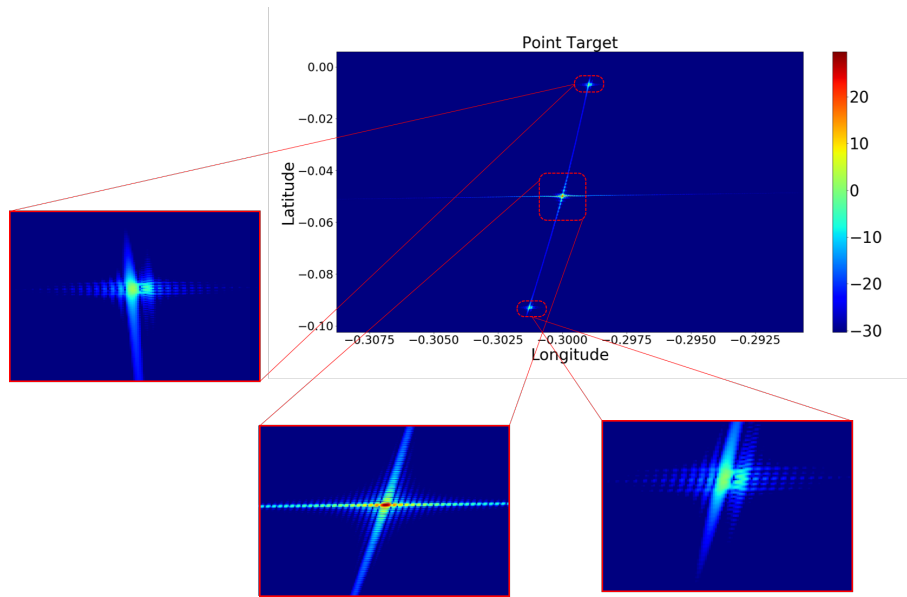
Figure 5.18: Enhanced depiction of the point target and first order ambiguities for beginning of sub-swath 1, AASR = -20.83 dB

End of Sub-Swath 1
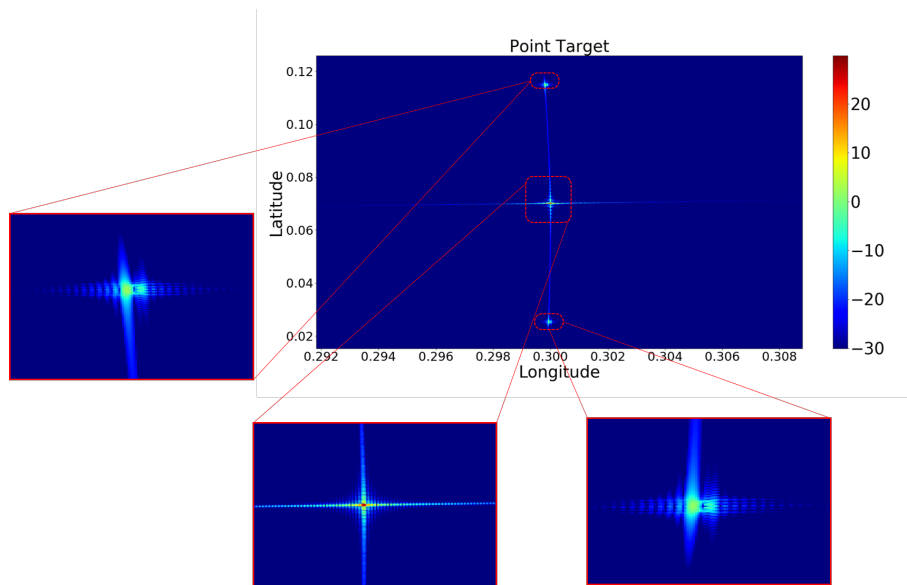
Figure 5.19: Enhanced depiction of the point target and first order ambiguities for end of sub-swath 1, AASR = -21.37 dB

Beginning Sub-Swath 2
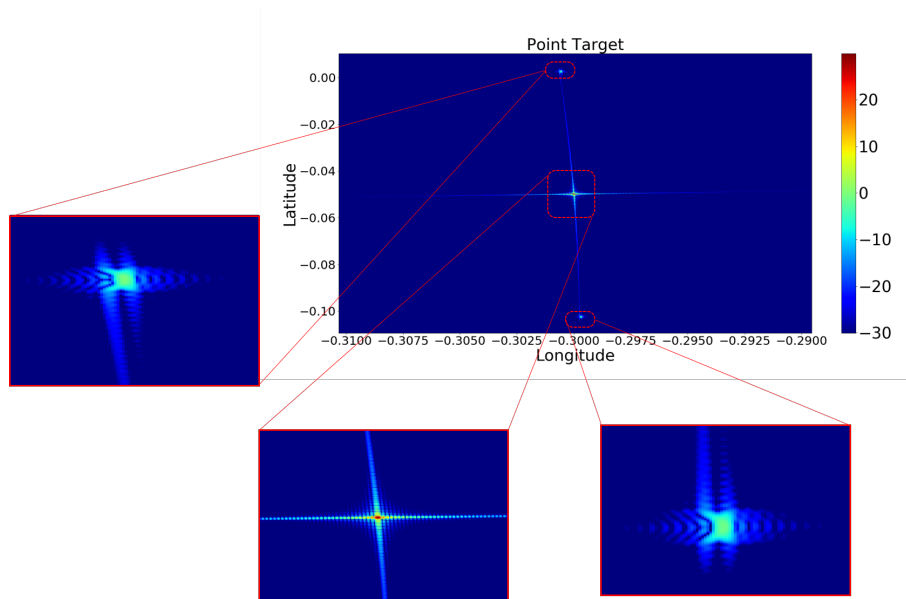
Figure 5.20: Enhanced depiction of the point target and first order ambiguities for beginning of sub-swath 2, AASR = -23.46 dB

End Sub-Swath 2
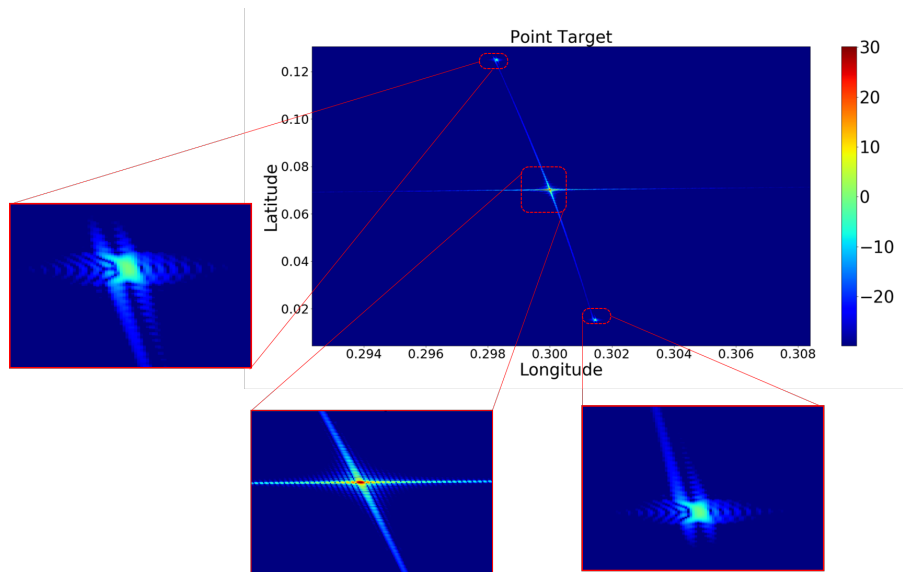
Figure 5.21: Enhanced depiction of the point target and first order ambiguities for end of sub-swath 2, AASR = -24.01 dB

Three subswaths are considered for this analysis which is depicted from Fig. 5.10 to 5.21.The simulations are for a point target which is placed at the beginning and end of every sub swath. Ambiguities of first order can be observed and the ambiguities are not centered due to different incidence angles and PRF. From eqn. 5.1, it can be noted that position of ambiguities depend on PRF, hence the change in position. The intensity of one of the ambiguities is slightly better (ref. Fig. 5.10 and Fig. 5.14)and are not identical as the pattern is asymmetrical and the phase history of the ambiguities are not the same. The influence of the ambiguities on the SAR data can be determined by AASR.

5.4.1 Pointing Error

Pointing errors can be introduced into the system due to the shaking of internal mechanism and external environmental factors which can have its effects on the platform stability of SAR [29]. This can affect the quality of images after processing, hence it is important to analyse pointing errors. This section deals with the pointing errors that are introduced in the receiver antenna along the (u axis) the azimuth plane of the antenna. The pointing error u is induced by deviation in antenna rotation around v or the elevation direction. This is analysed for both beamforming on ground and beamforming on board which is depicted in the following simulations.

Beamforming on Ground
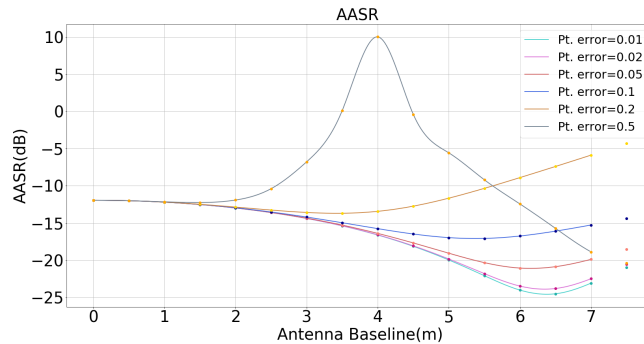
(a) AASR for subswath 0
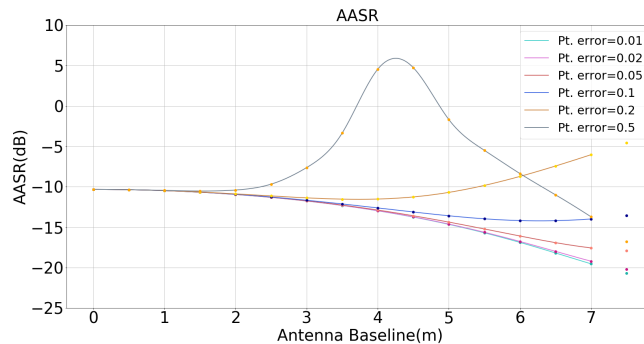
(b) AASR for subswath 1
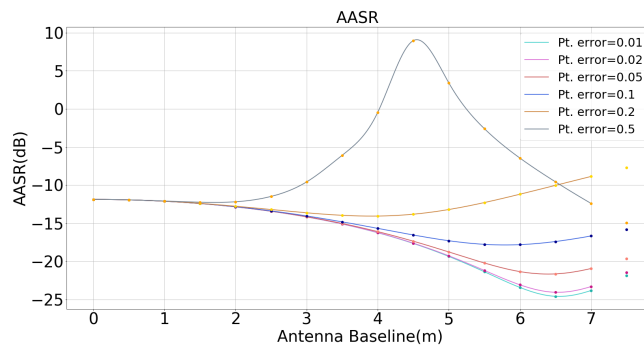
(c) AASR for subswath 2

Figure 5.22: The AASR computed for beamforming on ground and for different subswaths. AASR is plotted against antenna baseline varying from 0 m to 7 m for different pointing errors.

Beamforming on Board
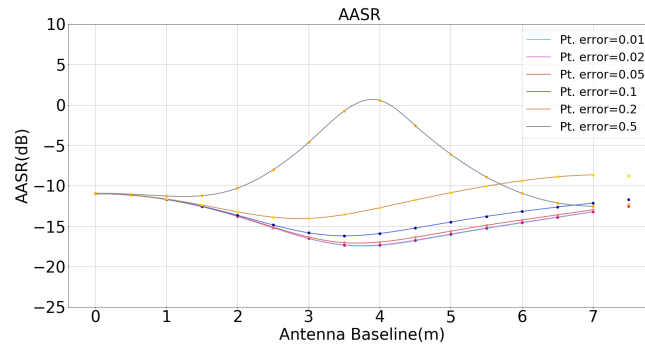
(a) AASR for subswath 0
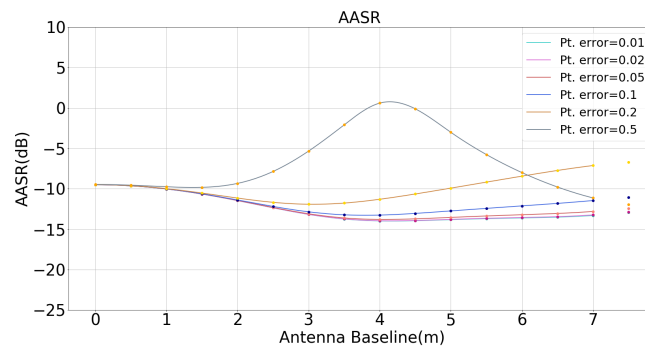
(b) AASR for subswath 1
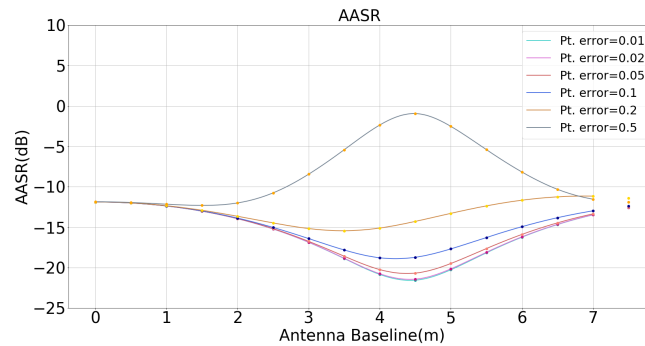
(c) AASR for subswath 2

Figure 5.23: The AASR computed for beamforming on-board and for different subswaths. AASR is plotted against antenna baseline varying from 0 m to 7mfor different pointing errors.

The above figures simulated for beamforming on ground the behaviour of the simulator can be observed for different baseline configurations. For a baseline from 0 to 1 m , the AASR value remains constant, but the magnitude changes for different subswath due to the change in PRF. As the antenna baseline increases the lobes of the antenna pattern become narrower, so when the antenna is pointing at the target, the target may fall in the null region of the antenna pattern. Therefore, a peak is observed in the AASR when the antenna of a specific baseline points at a null region. The antenna baseline of 4 m to 5 m provides an optimum performance and its sensitivity to pointing errors also increases. The errors induced at higher baselines is higher than those at smaller baselines. It can be concluded that the ability of the antenna to handle higher pointing error lies between antenna baseline 4 and 5 meters hence it is more favorable. It can be noted that AASR of upto 10 dB can be handled by beamforming on ground and a maximum of 2 dB AASR

can be handled by beamforming on board. Considering the ideal values of AASR (-15dB to -20 dB), the optimum baseline slightly varies between 4 m and 5 m.

5.4.2 Gain Imbalances

Gain Imbalances are the imperfect constant amplitude changes introduced in the STEREOID receiver antenna. The effect of gain imbalances are observed when estimating the position of targets, i.e, there may be a wrong estimation of target position and can affect the focusing process involved in SAR.
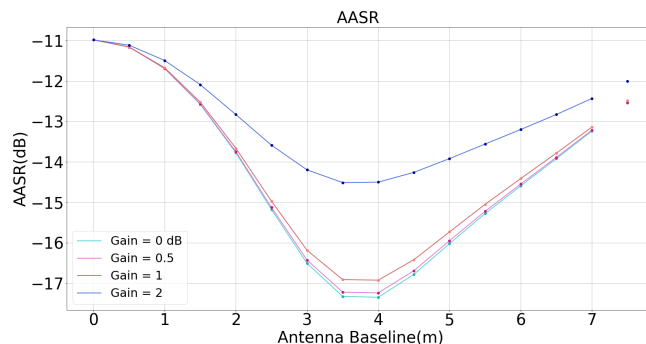
Figure 5.24: Evaluation of AASR for different amplitude gains introduced on the STEREOID receiver antenna for different antenna baseline configuration. The evaluation was performed for beamforming on-board and for the sub-swath 0 for 0 pointing errors.

From the above Fig. 5.24 it can be noted that for beamforming on-board, for gain = 0 dB and 0 pointing errors, the system behaves normally for all values of AASR. As a constant amplitude change is introduced into the system, then the amplitude of AASR increases. If the introduction of imperfect gain amplitude continues to grow higher and higher, then the system behaves like a large single antenna and the directivity of the antenna reduces, hence a gain imbalance of less than 2 dB is tolerable.

5.4.3 Comparison of Beamforming on Ground and Beamforming on–board

The simulations performed for various case scenarios for beamforming on ground and beamforming on-board provides information on the behaviour of the system. Theoretically, as presented in Chapter 4, beamforming on ground is better as the phase can be controlled and directed to point the target. Beamforming on-board cannot precisely point to the target but scans from beginning to end of scene for a desired time duration. From the above simulations, conclusions can be drawn that beamforming on ground is more precise and accurate than that on-board. This is evident from the temporal patterns for both cases. The magnitude difference for temporal pattern on ground is better than that on-board. Further, the AASR values for beamforming on ground were lesser than that on board. The introduction of pointing errors can be handled better on ground than that on-board. The effect gain imbalances decreased the performance of on-board processing as the gain increases. The study requires further investigation to draw more conclusions.

5.5 CONCLUSIONS AND FUTURE SCOPE

The resolution of the focuser was described in Chapter 3 and the focuser had close to ideal values of resolution in both range and azimuth, i.e., around 4.8 m and 21.31 m respectively for an along track baseline of 250km. The dual antenna configuration for STEREOID follows an elevation plane

alignment to avoid heavy squinted illuminations. Further, beamforming on ground and beamforming on-board were described for STEREOID. This chapter elaborates on performance analysis of the beamforming methods described. The analysis is performed for different antenna baseline configurations and the temporal pattern and time integration pattern were observed. The evaluation was conducted mainly based on AASR which is a parameter that determines the influence of ambiguities on the SAR image. It can be concluded from the observation that the performance of beamforming on ground is better. To support the analysis, the targets were placed at the beginning and end of every subswath which shows that AASR for beamforming on ground is better without any pointing errors.The gain imbalances for beamforming on ground were always optimum and do not change as the phase and pointing direction can be controlled. Gain imbalances of between 0dB to 1dB is optimal for beamforming on-board. The optimal antenna baseline seem to change slightly due to the different behaviour of the antenna pattern in time but this area requires more investigation.

The future scope of the thesis lies in the extending the analysis to moving targets. The simulator can be extended to multistatic mode and different flight formation configurations. Based on the performance analysis, it can be concluded that calibration errors can lead to a degraded imaging quality. Hence different algorithms can be explored to mitigate calibration errors.

BIBLIOGRAPHY

[1] Ian G. Cumming and Frank H. Wong, *Digital Processing of Synthetic Aperture Radar Data - Algorithms and Implementation*, Artech House, Boston, 2005.

[2] Li Zhuo, Li Chunsheng, YuZe, Zhou Jian, Chen Jie, *Backprojection algorithm for high resolution Geo-SAR Image Formation*, IGARSS 2011

[3] Antonio Moccaia and Alfredo Renga, *Chapter 1, Bistatic Synthetic Aperture Radar*, Distributed Space Missions for Earth System Monitoring, Microcosm Press El Segundo, California

[4] Manfred Zink, Gerhard Krieger, Hauke Fiedler, Irena Hajnsek, Alberto Moreira, Marian Werner, *TanDEM-X – The First Bistatic SAR Formation in Space*,Advanced RF Sensors for Earth Observation (ARSI), September 2011

[5] Paco Lopez Dekker, Helmut Rott, Bertrand Chapron, Pau Prats-Iraola, *Stereo Thermo-Optically Enhanced Radar for Earth, Ocean, Ice, and land Dynamics (STEREOID)*, Research Proposal, March 2018

[6] Don Koks, *Using Rotations to Build Aerospace Coordinate Systems*, Electronic Warfare and Radar Division Systems Sciences Laboratory, Australian Government, Department of Defence

[7] Francesco De Zan and Andrea Monti Guarnieri, *TOPSAR : Terrain Observation by Progressive Scans*, IEEE Transactions on Geoscience and Remote Sensing, September 2006

[8] Airbus Defence and Space, *TerraSAR-X Image Product Guide, Basic and Enhanced Radar Satellite Imagery*, Issue 2.1, March 2015

[9] German Aerospace Center(DLR),*Microwaves and Radar Institute, Status Report 2000-2005*, April 2006

[10] Marc Rodriguez-Cassola ; Stefan V. Baumgartner ; Gerhard Krieger ; Alberto Moreira, *Bistatic TerraSAR-X/F-SAR Spaceborne–Airborne SAR Experiment: Description, Data Processing, and Results*, IEEE Transactions on Geoscience and Remote Sensing (Volume: 48 , Issue: 2 , Feb. 2010)

[11] Manfred Zink, Hauke Fiedler, Irena Hajnsek, Gerhard Krieger, Alberto Moreira, Marian Werner , *The TanDEM-X Mission Concept*, Geoscience and Remote Sensing Symposium, 2006. IGARSS 2006, September 2006

[12] ESA Earth Online, *TerraSAR-X / TanDEM-X, Mission Facts and Figures*, https://earth.esa.int/web/guest/missions/3rd-party-missions/current-missions/terrasar-x

[13] Yew Lam Neo (2007), *Digital Processing Algorithms for Bistatic Synthetic Aperture Radar Data*(Doctoral Thesis), The University of British Columbia, Canada.

[14] Don Koks,textitUsing Rotations to Build Aerospace Coordinate Systems, Electronic Warfare and Radar Division Systems Sciences Laboratory, Australian Government, Department of Defence.

[15] Nicolas Gebert, Bernardo Carnicero Domínguez, Malcolm W. J. Davidson, Marina Diaz Martin, Pierluigi Silvestrin, *SAOCOM-CS – A passive companion to SAOCOM for single-pass L-band SAR interferometry*, EUSAR, 2014.

[16] Helmut Rott, Paco Lopez Dekker, Svein Solberg, Lars Ulander, Thomas Nagler, Gerhard Krieger, Pau Prats, Marc Rodriguez, Mariantonietta Zonno, Alberto Moreira, *SESAME: A single-pass interferometric SEntinel-1 companion SAR mission for monitoring GEO- and biosphere dynamics*, IEEE International Geoscience and Remote Sensing Symposium (IGARSS), 2017

[17] Marc Rodriguez-Cassola, Pau Prats-Iraola, Francesco De Zan, Rolf Scheiber, Andreas Reigber, Dirk Geudtner and Alberto Moreira, *Doppler-Related Distortions in TOPS SAR Images*, IEEE Transactions on Geoscience and Remote Sensing, January 2015.

[18] Bai Xia, Sun Jin Ping, Hong Wen, Mao Shi Yi, *On the TOPS mode spaceborne SAR*, Science China Press and Springer-Verlag Berlin Heidelberg 2010, February 2010

[19] Adele Fusco, Antonio Pepe, Paolo Berardino, Claudio De Luca, Sabatino Buonanno, and Riccardo Lanari, *A Phase-Preserving Focusing Technique for TOPS Mode SAR Raw Data Based on Conventional Processing Methods*, Sensors(Basel), Jul 29, 2019

[20] Qianghui Zhang, Junjie Wu, Zhongyu Li, Yulin Huang, Jianyu Yang and Haiguang Yang, *On the Spatial Resolution Metrics of Bistatic SAR*, 2016 CIE International Conference on Radar (RADAR), October 2016

[21] Antonio Moccia and Alfredo Renga, *Spatial Resolution of Bistatic Synthetic Aperture radar: Impact of Acquisition Geometry on Imaging Performance*, IEEE Transactions on Geoscience and Remote Sensing, October 2011

[22] Wikipedia, *WGS 84*, $https://nl.wikipedia.org/wiki/WGS_84$, 10 Jan, 2018

[23] Tore Lindgren, *Algorithm Development for Multistatic GNSS Radar Technology*, Licentiate Thesis, 2007:29.

[24] M. D'Errico ; A. Moccia, *Attitude and antenna pointing design of bistatic radar formations*, IEEE Transactions on Aerospace and Electronic Systems, July 2003

[25] Erik De Witte, Attitude laws for Bistatic SAR Companion Satellites, Personal Communication, 26 June 2019

[26] M. Younis, C. Fischer and W. Wiesbeck, *Digital beamforming in SAR systems*, IEEE Transactions on Geoscience and Remote Sensing, 18 August 2003.

[27] Michelangelo Villano and Gerhard Krieger, *Spectral- Based Estimation of the Local Azimuth Ambiguity-to-Signal Ratio in SAR images*, IEEE Transactions on Geoscience and Remote Sensing, May 2014.

[28] Michelangelo Villano and Gerhard Krieger, *Impact of Azimuth Ambiguities on Interferometric Performance*, IEEE Transactions on Geoscience and Remote Sensing, September 2012

[29] X. Zhang, S.J.Liu, H.F.Yu, X.H.Tong, G.M.Huang, *Effect of Antenna Pointing errors on SAR imaging considering the change of point target location*, ISPRS Annals of the Photogrammetry, Remote Sensing and Spatial Information Sciences, Volume IV-3, 2018.

[30] Hui Meng, Jinsong Chong, Yuhang Wang, Yan Li and Zhuofan Yan, *Local Azimuth Ambiguity-to-Signal Ratio Estimation Method Based on the Doppler Power Spectrum in SAR Images*, Remote Sensing Journal, 9 April, 2019.

[31] Mingyang Shang, Xiaolan Qiu, Bing Han, Chibiao Ding and Yuxin Hu , *Channel Imbalances and Along-Track Baseline Estimation for the GF-3 Azimuth Multichannel Mode*, remote sensing Journal, 2019